Chapter 5
Rare Earth Based Anisotropic Nanomaterials: Synthesis, Assembly, and Applications

Chun-Hua Yan, Ling-Dong Sun, Chao Zhang, Chun-Jiang Jia, Guang-Ming Lyu, Hao Dong, Xiao-Yu Zheng, Yan-Jie Wang, Shuo Shi, Pei-Zhi Zhang and Lin-Dong Li

Abstract Rare earths (RE) refer to the lanthanide elements La–Lu together with Sc and Y. Conventionally, they have found applications in phosphors, magnets, catalysts, fuel cell electrodes/electrolyte. Here in this chapter, we discuss the synthesis, assembly and applications of rare earth based anisotropic nanomaterials. Regarding synthesis, the anisotropic growth behaviors of these nanocrystals are predominantly governed by their own unique crystal structures. Yet for wet-chemistry synthetic methods where a number of parameters could be finely tuned, the addition of particular coordination agents, templating agents or mineralizers has proven to be an effective way to direct the growth of nanocrystals into some anisotropic structures. Regarding applications, anisotropic nanomaterials, compared to their isotropic counterparts, often exhibit distinct properties. For example, the luminescence of anisotropic nanomaterials can display polarization and site-specific features. As for rare earth nanomaterials as magnetic resonance imaging (MRI) contrast agents, the high surface area of anisotropic nanostructures can give rise to superior performances. And for catalysis applications, anisotropic nanomaterials expose rich, highly active facets, which is of great importance for facet-selective catalytic reactions. In the chapter, we will start with introduction of the crystal structures of rare earth compounds, then briefly summarize the synthesis and assembly of rare earth anisotropic nanomaterials, and discuss their properties and applications in three realms, namely, luminescence, magnetism and catalysis.

C.-H. Yan (✉) · L.-D. Sun · C. Zhang · G.-M. Lyu · H. Dong · X.-Y. Zheng · Y.-J. Wang
S. Shi · P.-Z. Zhang · L.-D. Li
Beijing National Laboratory for Molecular Sciences, State Key Laboratory of Rare Earth Materials Chemistry and Applications, PKU-HKU Joint Laboratory in Rare Earth Materials and Bioinorganic Chemistry, College of Chemistry of Molecular Engineering, Peking University, Beijing, China
e-mail: yan@pku.edu.cn

C.-J. Jia
School of Chemistry and Chemical Engineering, Shandong University, Jinan, China

Q. Li (ed.), *Anisotropic Nanomaterials*, NanoScience and Technology,
DOI 10.1007/978-3-319-18293-3_5

5.1 Crystal Structures of Rare Earth Compounds

5.1.1 Rare Earth Oxides

As rare earth elements show strong affinity to oxygen, they can be easily synthesized in the air, and rare earth oxides enjoy the most investigation among its solid compounds. Rare earth oxides mostly take the form of sesquioxides (RE_2O_3) due to their trivalency, while some elements can also exist as divalent or tetravalent ions in their oxides, thus forming monoxides, dioxides or mixed valence oxides with a complex crystal structure [1]. Europium and ytterbium monoxides are the only two rare earth monoxides that are stable in solid form, and they are readily oxidized in the air. Praseodymium and terbium usually exist as both trivalent and tetravalent ions in their oxides, thus forming mixed valence oxides with non-stoichiometric formulas of Pr_6O_{11} and Tb_4O_7, respectively. Cerium exists exclusively as tetravalent ions in its most stable oxide, CeO_2 [2].

Rare earth sesquioxides are the most common category of rare earth oxides. Depending on their cationic radii, rare earth sesquioxides can be most stable in hexagonal phase (A phase), monoclinic phase (B phase) or body-centered cubic phase (C phase) under ambient conditions (as shown in Fig. 5.1). In both hexagonal (A phase) and monoclinic (B phase) sesquioxides, a rare earth cation is coordinated by seven oxygen ions, with six oxygen ions forming an octahedron around the cation. In hexagonal sesquioxides, the last oxygen ion rests on one of the octahedron's faces, while in monoclinic sesquioxides, the last oxygen ion locates exceptionally far from the cation. Light rare earth sesquioxides such as La_2O_3, Ce_2O_3, Pr_2O_3 and Nd_2O_3 usually exist in hexagonal phase due their large cationic radii, while Sm_2O_3 usually takes monoclinic phase due to its smaller cationic radius. In body-centered cubic (C phase) sesquioxides, a rare earth cation is coordinated by six oxygen ions, resembling a cubic fluoride structure with two anions removed. The cation occupies two different kinds of vacancies formed by differently removed surrounding anions. Y_2O_3 and all lanthanide oxides heavier than Sm_2O_3 (Eu_2O_3 to Lu_2O_3) exist in C phase.

EuO and YbO have a cubic halite structure and the space group *Fm3m* with the cation coordinated by six oxygen ions. The monoxides can also be mixed with the corresponding sesquioxides in 1:1 ratio to form the mixed valence oxides of Eu_3O_4 and Yb_3O_4, respectively.

As one of the most studied rare earth compound, CeO_2 is a notable exception to the sesquioxide norm. CeO_2 has a cubic fluorite structure and the space group *Fm3m*, with the cation coordinated by eight oxygen atoms. As the valence of cerium can alternate between Ce(III) and Ce(IV), Ce^{4+} in the lattice can be reduced to Ce^{3+} under reductive conditions, accompanied by the generation of oxygen vacancies that serve as highly active catalytic sites and oxygen storage centers. Despite the formation of Ce^{3+}, CeO_2 can maintain its cubic fluorite structure under intense reduction. This excellent chemical stability combined with its thermal stability makes it a versatile catalyst and oxygen sensor under rigorous conditions [3].

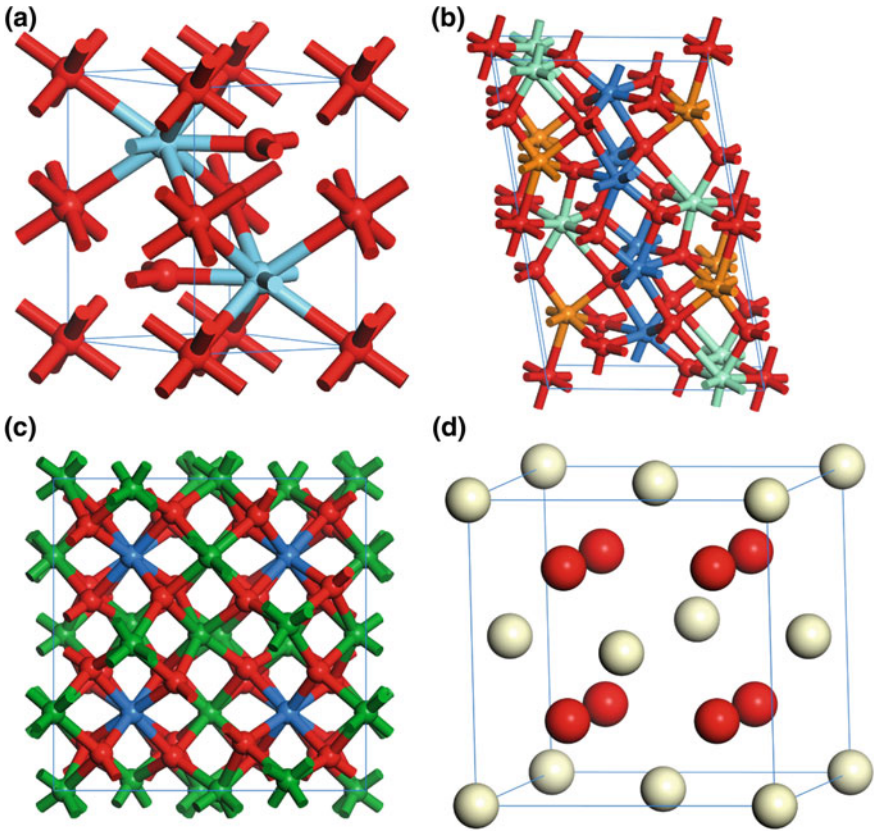

Fig. 5.1 Crystal structures of rare earth oxides. **a** Hexagonal sesquioxide. *Blue spheres* denote RE^{3+}; *red sphere* O^{2-}. **b** Monoclinic sesquioxide. *Blue*, *green* and *orange spheres* denote RE^{3+} in three different coordination environments; *red spheres* O^{2-}. **c** Cubic sesquioxide unit cell projected along the *c* axis. *Blue* and *red spheres* denote RE^{3+} in two different coordination environments; *red spheres* O^{2-}. **d** Cubic fluorite CeO_2. *White spheres* denote Ce^{4+}; *red spheres* O^{2-}

PrO_2 and TbO_2 also possess a cubic fluorite structure similar to CeO_2. The sesquioxides of praseodymium and terbium adopt a body-centered cubic structure as described above, enabling them to mix with their cubic fluorite dioxides to form mixed valence oxides.

5.1.2 Rare Earth Fluorides

Binary rare earth fluoride REF_3 has two kinds of crystal structures: trigonal fluocerite structure and orthorhombic β-YF_3 structure. Trigonal REF_3 has a

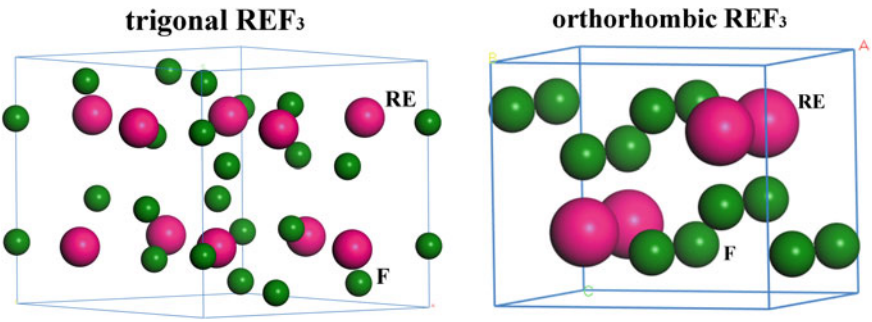

Fig. 5.2 Crystal structures of trigonal REF_3 and orthorhombic REF_3 (built by CERIUS2 software (http://www.accelrys.com/cerius2)

hexagonal phase with the space group of *P*-3*c1*. The rare earth cations lie on a twofold rotation axis. There are nine fluorine atoms near each rare earth atom. The distance of RE^{3+} and F^- ions is between 0.242 and 0.264 nm. There are two F^- ions far from the RE^{3+} ions with a distance of 0.301 nm. Rare earth atom is nine-coordinated via 9 fluorine atoms. Each F^- anion bonds with three RE^{3+} cations in a three-bridged configuration. β-YF_3 belongs to orthorhombic structure, *Pnma* space group. In this system, it is a three-dimensional (3D) network molecule with a F^- anion as a bridged atom. Each F^- anion bonds with three Y^{3+} as three bridges. There are nine F^- anions coordinated with Y^{3+}, eight of them close to the Y, while the other one is a little far. The nine F^- anions form a triangular prism coordination polyhedron (shown in Fig. 5.2).

REF_2 has a cubic fluorite structure, *Fm3m* space group. REF_2 can produce some complex fluorides. EuF_2 and CsF can form perovskite $CsEuF_3$. EuF_2 and MgF_2 can form orthogonal $SmMgF_4$ and $EuMgF_4$. EuF_2 and AlF_2 can form cubic solid solution (Eu, Al) $F_{2.00\text{-}2.44}$ and tetragonal system $EuAlF_5$. EuF_2 can form $EuZrF_6$, $EuSiF_6$, $EuThF_6$ with ZrF_4, SiF_4 and ThF_4 respectively.

5.1.3 Rare Earth Complex Fluorides

According to the coordination states of rare earths, the rare earth complex halide A_mREX_n (A = alkali and/or alkaline earth metal; RE = rare earth; X = halide) compounds can take the following forms: (1) $AREX_4$, a fourfold coordination of rare earth cations is accompanied by twofold or threefold coordination of the alkali and/or alkaline earth atom. (2) A_2REX_5, rare earth cations are in a fivefold coordination configuration, energetically more stable than a fourfold one. (3) A_3REX_6, the fivefold and sixfold coordination of rare earth cations are energetically competitive. For both A_2REX_5 and A_3REX_6, each coordination state can be realized in various forms that differ in detail but are close in energy.

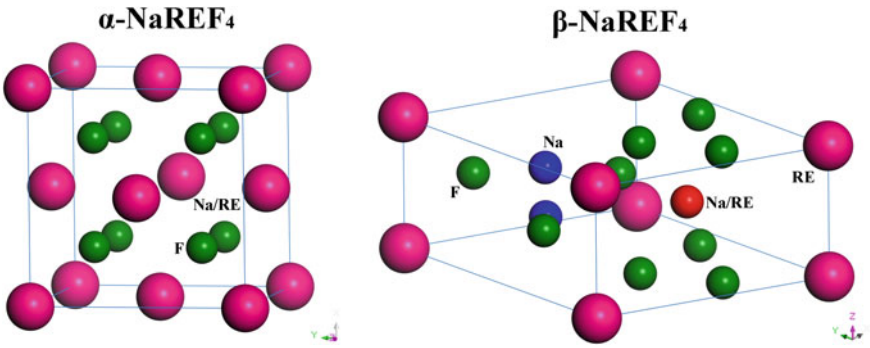

Fig. 5.3 Crystal structures of α-$NaREF_4$ and *β*-$NaREF_4$ built by CERIUS2 software (http://www.accelrys.com/cerius2)

Common structure types of the $AREF_4$ include tetragonal anti-scheelite ($LiYF_4$), hexagonal ($NaNdF_4$), trigonal ($KErF_4$), and orthorhombic ($KCeF_4$) type [4–6]. In addition, a high-temperature modality exists which has A^+ and RE^{3+} cations at the Ca^{2+} sites of cubic CaF_2 structure with statistical distribution.

As shown in Fig. 5.3, α-$NaREF_4$ has a cubic phase with the space group of *Fm3m*. *β*-$NaREF_4$ has a hexagonal phase (space group: *P*-6 *or* $P6_3/m$). In the cubic-phase α-$NaRF_4$, Na^+ and RE^{3+} cations are randomly distributed in the cationic sublattice. In the hexagonal-phase β-$NaREF_4$, the cation sites contain three types: a onefold site occupied by RE^{3+}, a onefold site occupied randomly by 1/2 Na^+ and 1/2 RE^{3+}, and a twofold site occupied randomly by Na^+ and vacancies [7].

5.1.4 Rare Earth Oxyhalides

Rare earth oxyhalides have two structures: tetragonal phase (*P4/nmm* space group) and trigonal phase (*R3m* space group), as shown in Fig. 5.4 [8, 9]. In the tetragonal phase, RE^{3+} cations occupy the position with C_{4v} symmetry. The tetragonal phase is thermodynamically less stable, and tends to form nonstoichiometric compounds with more complex structures. In the hexagonal phase, RE^{3+} cations occupy the position with C_{3v} symmetry. At high temperature, the hexagonal phase can transform into cubic structure.

5.1.5 Rare Earth Phosphates and Vanadates

For rare earth orthophosphates ($REVO_4$), there exist four different phases, mostly depending on the cationic radius of rare earth element: monazite, xenotime, rhabdophane, and churchite [10]. Rare earth orthovanadates ($REVO_4$) have two

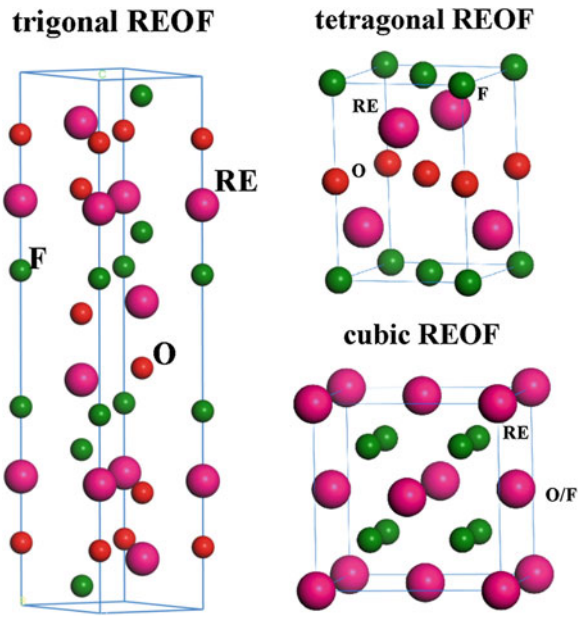

Fig. 5.4 Crystal structures of trigonal REOF, tetragonal REOF and cubic REOF built by CERIUS2 software (http://www.accelrys.com/cerius2)

isomorphic phase structures, namely, monoclinic (*m*-) monazite type, and tetragonal (*t*-) zircon type. The phase selectivity for $REVO_4$ relies on the radius of RE^{3+}, only zircon type is observed for all rare earth orthovanadates excluding $LaVO_4$ and $CeVO_4$ that can crystallize in both monoclinic and tetragonal phased structure [11, 12].

5.2 Synthesis, Assembly of Rare Earth Based Anisotropic Nanomaterials

5.2.1 One-Dimensional (1D) Nanostructures

One-dimensional (1D) nanostructures include nanorods, nanowires, and nanotubes. Many solid materials naturally grow into 1D nanostructures, the growth direction of which is usually dominated by the crystallographic symmetry [13–17]. However, rare earth oxides often have isotropic structures; for example, CeO_2 crystals has a face-centered cubic (fcc) structure (space group: *Fm3m*). Therefore, CeO_2 nanocrystals tend to present high-symmetry morphologies, such as cubes and octahedra. To obtain low-symmetry morphologies, templating or capping agents are generally needed to differentiate the surface energy of each facet and to direct anisotropic growth and the formation of 1D structures. Therefore, various templating methods have been established for preparing CeO_2 nanorods and nanowires. Porous anodic

alumina membranes (AAM) are commonly used in such synthesis as hard templates by virtue of their modulated pore diameters, ideally rod-shaped pores and exceptionally narrow size distribution [18–20]. CeO_2 nanowires were successfully synthesized with an improved sol–gel method within the hexagonally ordered nanochannels of the AAM. Ce^{3+} cations and corresponding anions reacted directly inside the nanochannels to form intermediates with 1D nanostructures. After post-treatment, the intermediates were transformed into the arrays of CeO_2 nanowires within the pores of AAM template [20].

CeO_2 nanorods can also be synthesized with solvothermal/hydrothermal methods [21–23], which generally feature controlled composition and morphology, low aggregation and high crystallinity, because of the diffusion-controlled growth in solvent media in a closed system. Yan's group prepared high-aspect-ratio ceria nanorods through a facile hydrothermal treatment without addition of any templates [24]. Using $Ce(NO_3)_3$ as the precursor, hexagonal $Ce(OH)_3$ intermediate was formed in the presence of OH^- anions (6 mol L^{-1}). After drying, white $Ce(OH)_3$ nanocrystals were converted into yellow $CeO_2 \cdot nH_2O$ in ambient atmosphere, without any change in their shape. Very recently, Yan's group have obtained lanthanide-doped CeO_2 nanowires through a modified hydrothermal route in the presence of NaOH and NaCl without any additional capping agents (as shown in Fig. 5.5) [25]. Such preparation process can be described with the following equations:

$$Ce^{3+}_{(aq)} + xLn^{3+}_{(aq)} + yOH^-_{(aq)} \rightarrow Ce(OH)_3{:}x\%Ln_{(s)} \tag{5.1}$$

$$Ce(OH)_3{:}x\%Ln_{(s)} + yO_{2(g)} \rightarrow CeO_2{:}x\%Ln_{(s)} + zH_2O \tag{5.2}$$

In this approach, Ce^{3+} precursor was dissolved in a high-concentration alkaline solution, forming one-dimensional $Ce(OH)_3$ intermediates with hexagonal structure. Upon calcination at 300 °C for 1 h, the nanowires transformed into CeO_2:Ln nanowires without prominent change in shape.

Zink's group reported a facile template-free hydrothermal method to obtain hierarchical architectures of CeO_2 nanorods in an acidic medium (as shown in Fig. 5.6) [26]. Na_3PO_4, as a mineralizer, plays a key role in controlling the morphology of CeO_2 nanostructures by adjusting the electrostatic potential and surface energy of CeO_2 nanorods. They investigated the mechanisms of nucleation and crystal growth process by varying the cerium precursors and concentration, concentration of phosphate, reaction temperature, pH of the reaction mixture, seeding and secondary treatment. Aspect ratios of these CeO_2 nanorods and nanowires can be precisely controlled and finely tuned from 4.1 to more than 100. The single-crystalline CeO_2 nanorods/nanowires grew along the [211] direction by an "oriented attachment" mechanism, followed by Ostwald ripening. Both phosphate and chloride ions were critical to the synthesis of one-dimensional CeO_2 nanorods and nanowires in both primary and secondary hydrothermal process. The strong coordination effect of phosphate with cerium ions was the driving force for the

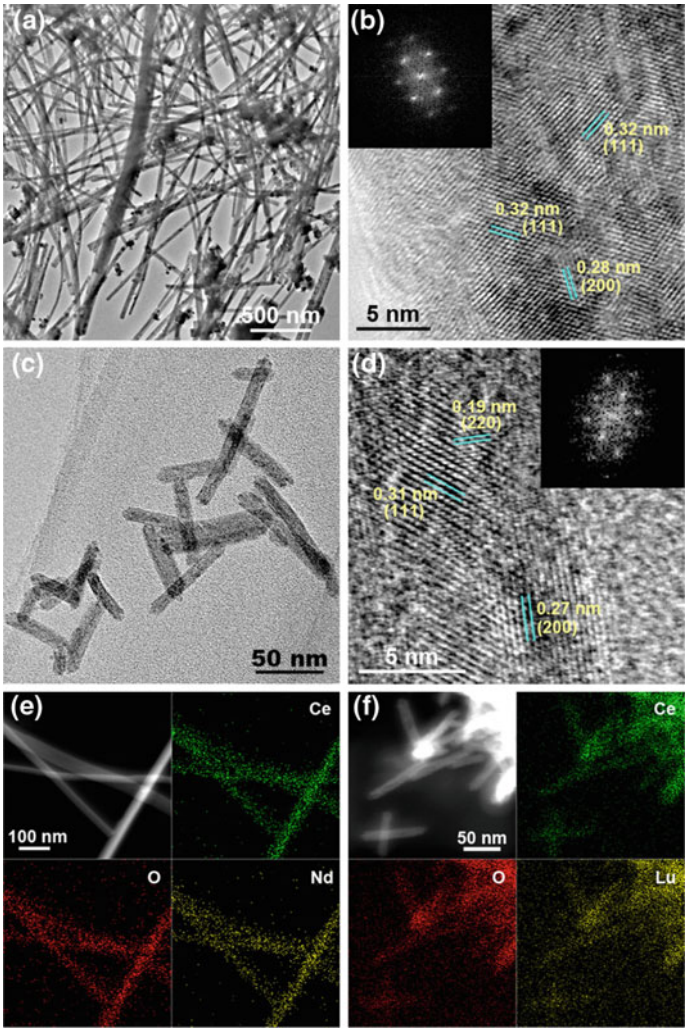

Fig. 5.5 TEM (**a**, **c**), HRTEM (**b**, **d**), and HAADF-STEM EDS elemental mapping (**e**, **f**) images of CeO_2:Nd (**a**, **b**, **e**) and CeO_2:Lu nanocrystals (**c**, **d**, **f**). (Reprinted with permission from [25]. Copyright 2013 American Chemical Society)

"dissolution" of nanorods under highly acidic condition. Chloride ions acted as a stabilizing agent in maintaining the rod/wire structure.

Rare earth oxide nanotubes have received extensive interests since the synthesis of carbon nanotubes in 1991 because they might offer unique properties and lead directly to original technological applications [27]. Han et al. first reported a facile method to synthesize CeO_{2-x} nanotubes by a hydrothermal route with mild reaction conditions [28]. By elevating the precipitation temperature and prolonging the

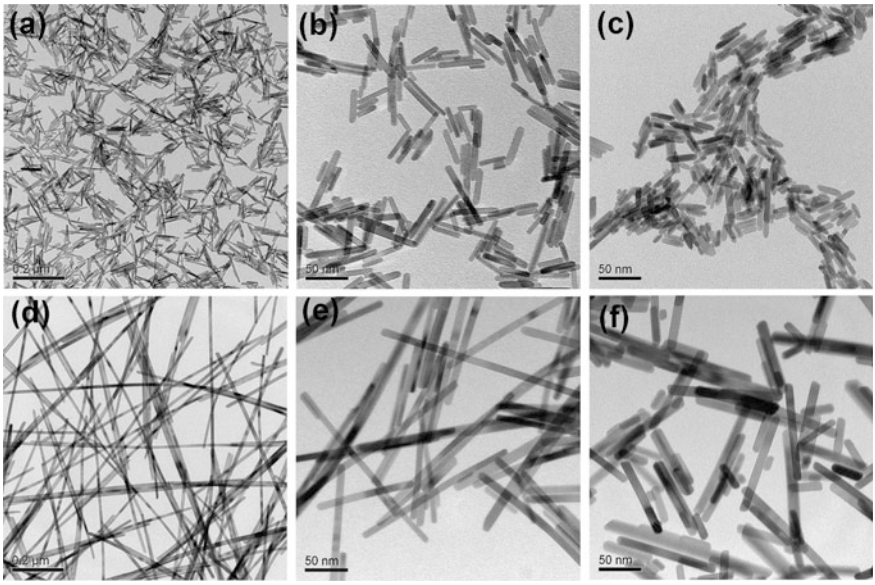

Fig. 5.6 TEM analyses of CeO_2 nanorods obtained from (**a**–**c**) primary and (**d**–**f**) secondary synthesis. (Reprinted with permission from [26]. Copyright 2012 American Chemical Society)

aging time, a large amount of nanotubes were formed. Nevertheless, this method had a few disadvantages, such as the time-consuming procedures, excessive by-products and difficulties for purification.

Yang's group developed an effective hydrothermal method to synthesize CeO_2 nanotubes with large cavities, thin walls and high quality [29]. A facile oxidation-coordination-assisted dissolution process of the hydroxide precursors was involved. First, $Ce(OH)_3$ nanowires were used as the starting materials; then the outer wall of $Ce(OH)_3$ nanostructures was partially oxidized by air. The oxidation-coordination-assisted dissolution process was limited inside the 1D nanomaterials. Finally, the ceria nanotubes with large cavities and thin walls were formed.

Chane-Ching et al. reported a general method for the synthesis of nanostructured materials with large surface area through the self-assembly of functionalized nanoparticles in a liquid-crystal phase [30]. Surface-functionalized ceria nanoparticles with the protonated amino acid interact directly with the ethylene oxide (CH_2CH_2O) groups of the copolymer. Based upon the weak interactions between the surfaces of the nanoparticles and the template, organized hexagonal arrays of CeO_2 nanoparticles are obtained and the symmetry of the arrays was preserved after calcination at 500 °C.

Seal et al. developed a very simple, green chemical route to guide self-assembly and time-dependent evolution of ceria nanoparticles into ultralong polycrystalline ceria nanorods [31]. By freezing and subsequent aging of an aqueous solution, CeO_2 nanoparticles trapped in voids (which form in ice) gradually evolve into

polycrystalline nanorods by localized oriented attachment process. MD simulations also predicted that the type of morphology evolution observed for the ceria nanostructures can be driven by the dimensional constraints.

Yan's group obtained four types of self-organized monolayer patterns (i.e., isolated particles, short chainlike (pseudo-1D aggregated), pearl necklace-like (1D aggregated), and dendritic (pseudo-2D aggregated) alignments during a PVP-assisted alcohothermal synthesis of ceria nanocrystals [32]. Possible self-organization mechanism of the nanosized CeO_2 colloids from isolated particle to 1D and 2D aggregated alignments were associated with the delicate balance of the attractive and repulsive forces caused by the adsorbed hydroxyls, PVP, and alkylammonium cations on the surfaces of CeO_2 nanocrystals during the irreversible evaporation of the solvent.

Using block copolymer Pluronic P123 as the template and ceric nitrate and zirconium oxide chloride as the precursors, highly ordered 2D hexagonal mesoporous $Ce_{1-x}Zr_xO_2$ solid solutions with a 2D hexagonal (p6mm) structure were synthesized via a novel direct and reproducible method as shown in Fig. 5.7 [33]. The overall synthesis strategy is based on a sol-gel process combined with evaporation-induced self-assembly in ethanol, without any extra reagents to adjust the pH of the sol-gel reaction. A series of mesoporous $Ce_{1-x}Zr_xO_2$ with different Ce/Zr ratios can be obtained under the optimized conditions, such as appropriate precursors, surfactants, and reaction temperature.

Nanosized rare earth fluorides and complex fluorides usually adopt plate-like morphologies due to their crystal structures, yet under certain conditions (for example, in the presence of shape-directing surfactants), 1D nanostructures can also be obtained. Chen et al. employed a precipitation method and prepared orthorhombic and hexagonal phase EuF_3 nanocrystals with various shapes, including nanospheres, nanobundles, nanorods, nanowires and nanoplates [34, 35]. Through a hydrothermal route, Li et al. obtained monodisperse LaF_3 and $NaLaF_4$ nanorods

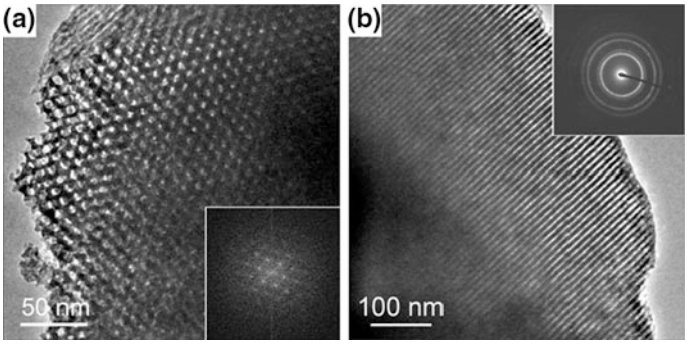

Fig. 5.7 TEM images of the mesoporous $Ce_{1-x}Zr_xO_2$ ($x > 0.5$) recorded along the **a** [001] and **b** [110] orientations. The *inset* in (**a**) is the corresponding FFT (fast Fourier transform) diffraction image, and the one in **b** is the corresponding SAED pattern. (Reprinted with permission from [33]. Copyright 2007 American Chemical Society)

with different aspect ratios [36]. They also developed a solvothermal method to prepare $NaYF_4$ nanocrystals by controlling the reactant concentration, temperature and duration, rod-like nanocrystals with good crystallinity and different sizes and aspect ratios were obtained [37–40]. Using YCl_3, NaF and EDTA as the starting materials, Qian et al. obtained spindle-like YF_3 with a hydrothermal method [41]. Interestingly, Zhao et al. discovered hexagonally ordered arrays of $NaYF_4$ nanotubes in a solvothermal reaction [42]. Yan's group developed a general thermolysis method to prepare rare earth fluorides and complex fluorides in high-boiling solvents (such as octadecene, oleic acid and oleylamine) using trifluoroacetate salts of rare earths and alkali metal; with proper ratio of Na to rare earth, hexagonal-phase $NaYF_4$ nanorods were obtained [43]. Using a similar approach, they obtained ultrathin EuOF nanowires with diameter below 2 nm [44]. The nanowires are highly flexible and can form ordered superstructures in a parallel configuration on substrates. A proper ratio of Eu precursor and surfactant oleic acid was found to be crucial for obtaining such wire-like structures.

For orthophosphates of light lanthanides (La–Gd), hexagonal rhabdophane and monazite phase rod-like or wire-like products could be obtained (as shown in Fig. 5.8) [45, 46]. With a temperature of l80–240 ºC, the products become the monazite phase with the morphology strongly affected by the acidity [47]. $LaPO_4$:Ln^{3+}(Ln^{3+} = Ce^{3+}, Tb^{3+}) and $LaPO_4$:Ce^{3+},Tb^{3+}/$LaPO_4$ core/shell nanowires have been synthesized on a large scale through a direct precipitation in a water-based system under moderate conditions without the assistance of any surfactant, catalyst, or template [48]. The diameters of the obtained nanowires are about 15 nm, and the lengths range from hundreds of nanometers to several micrometers. For heavy lanthanides (Ho–Lu) and Y, a synthesis temperature as low as 70 ºC is required to obtain hydrated monoclinic churchite phase, for example, YPO_4 nanowires [49]. Higher temperature leads to tetragonal zircon phase. Usually, a particle-like morphology is obtained with acidic conditions. When a chelating agent like EDTA is introduced, the hydrated hexagonal nanorods of YPO_4 could be obtained [50]. For intermediate lanthanides (Gd, Tb, Dy), hexagonal, tetragonal, and monoclinic phases may coexist. Therefore, results are more complex. Typically, rhabdophane type $TbPO_4$ nanorods form at low temperature and zircon type $TbPO_4$ nanocubes form at high temperature, both with acidic mother liquors [46]. Hexagonal $DyPO_4$ nanorod bundles form at low temperature [51]. Usually, the rhabdophane products of light rare earths convert to monazite products, while the churchite phase converts to zircon products with heat treatment [52].

Surfactants, chelating agents, as well as block copolymers are used to control the size and shape of rare earth phosphate nanocrystals. Bu et al. reported a P123-assisted hydrothermal synthesis of $CePO_4$:Tb single-crystalline thin nanorods of 10–12 nm in width. The surfactant Pluronic P123 was found to play a crucial role both to improve luminescence properties and nanorod homogeneity [53]. When the pH value of reaction system is adjusted to below 1.0, uniform spindle like nanowire bundles of $LaPO_4$ could be obtained [54]. Xing et al. reported the synthesis of uniform $CePO_4$ nanorods by reaction of aqueous [$(CTA)_3PO_4$] micelles with [Ce$(AOT)_3$] reverse micelles prepared in isooctane [55]. Ghosh et al. reported the

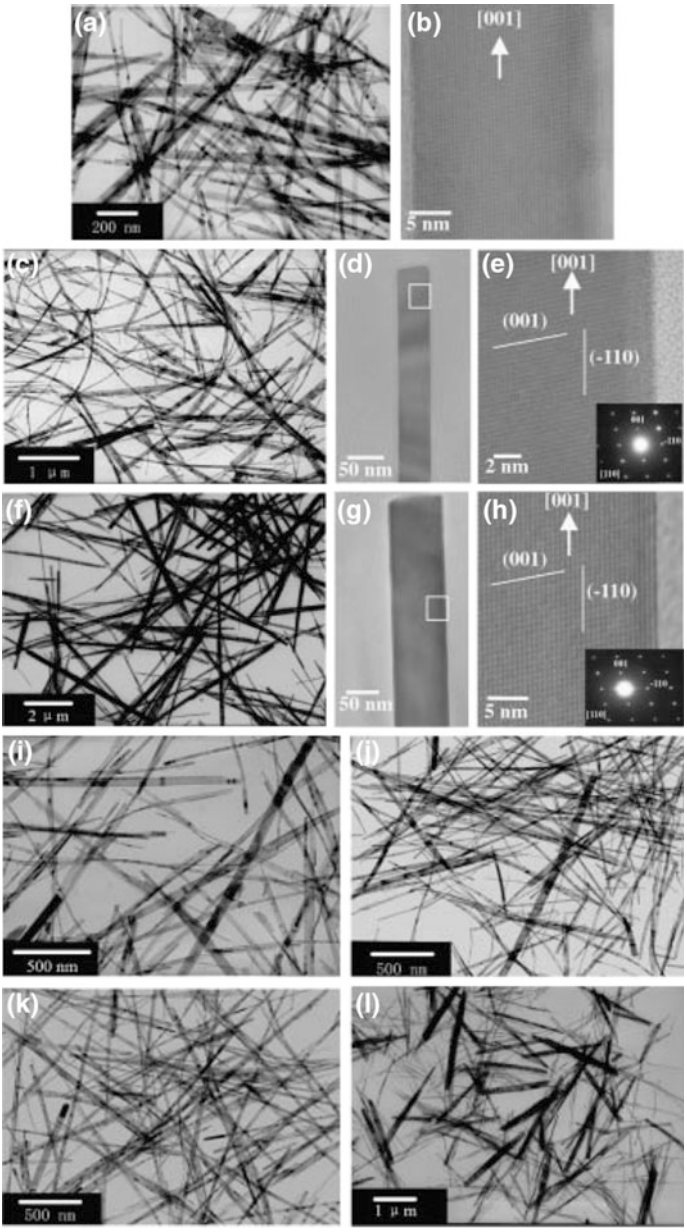
(a)
200 nm
(b)
[001]
5 nm
(c)
1 μm
(d)
50 nm
(e)
[001]
(001)
(-110)
2 nm
(f)
2 μm
(g)
50 nm
(h)
[001]
(001)
(-110)
5 nm
(i)
500 nm
(j)
500 nm
(k)
500 nm
(l)
1 μm

◀ **Fig. 5.8** **a** TEM image of $LaPO_4$ nanowires; **b** HRTEM image of a single 23 nm $LaPO_4$ nanowire; **c** TEM image of $SmPO_4$ nanowires; **d** TEM image of a uniform 50 nm $SmPO_4$ nanowire; **e** HRTEM image of a single $SmPO_4$ nanowire taken from the highlighted section with inset showing the electron diffraction pattern; **f** TEM image of $EuPO_4$ nanowires; **g** TEM image of a uniform 80 nm $EuPO_4$ nanowire; **h** HRTEM image of a single $EuPO_4$ nanowire taken from the highlighted section with inset showing the electron diffraction pattern; **i** TEM image of $CePO_4$ nanowires; **j** TEM image of $PrPO_4$ nanowires; **k** TEM image of $NdPO_4$ nanowires; and **l** TEM image of $GdPO_4$ nanowires/nanorods. (Reprinted with permission from [46]. Copyright 2003 Wiley-VCH.)

synthesis of $LaPO_4$:Er,Yb and $LaPO_4$:Er@$YbPO_4$ nanorods using a reverse micelles system [56]. Li et al. reported an OA-assisted solvothermal routes in mixed solution of water and ethanol for the synthesis of uniform hexagonal $REPO_4 \cdot nH_2O$ nanocrystals at 140 ºC (as shown in Fig. 5.9) [57]. The synthesis in high-boiling solvents gives out a number of advantageous features for the synthesis of doped $REPO_4$ nanocrytals. Yan et al. reported a series of high-quality dispersible $REPO_4$ nanocrytals with shapes of nanopolyhedra, quasinanorods, nanorods, and nanowires which are synthesized at 180–260 ºC in oleic acid and oleylamine solvents via a limited anion-exchange mechanism [58]. The assembly behavior during the synthesis of rare earth orthophosphates has been observed. Li et al. reported a one-pot synthesis of $CePO_4$ nanowires attached to CeO_2 octahedral micrometer crystals [59]. $Ce(NO_3)_3 \cdot 6H_2O$ and $(NH_4)_2HPO_4$ are used in a molar ratio of 2:1, pH value is tuned to be about 1, and the treatment temperature is 180 ºC. The photoluminescence properties of $CePO_4$ nanowires attached to CeO_2 octahedral micrometer crystals are enhanced strongly in comparison with pure $CePO_4$ nanowires.

For anisotropic orthovanadates, the first example reported is $LaVO_4$. Different from YVO_4 that only crystallizes in tetragonal phased structure, $LaVO_4$ exhibits both monoclinic and tetragonal phased structure. Therefore, phase modulation is the first task for the synthesis of $LaVO_4$-based materials. Wet chemistry routes always show superiority on the selective synthesis of nanomaterials with desired phase structure and morphology [60]. Sun et al. contributed several reports on this subject. In their synthesis, they used $NaVO_3$ and $La(NO_3)_3$ as the starting agents. The phase structure and morphology of $LaVO_4$ are dominated by aqueous pH value. Below pH 3.5, $LaVO_4$ crystallizes into irregular shaped *m*-phase nanoparticles. The *t*-phase nanorods only form in the pH range of 4.5–6.0. It is noticed that at early stage, $NaVO_3$ and $La(NO_3)_3$ solution were mixed to form a yellow suspension of *m*-$LaVO_4$. Then, the crude precipitates were transformed into *t*-$LaVO_4$ nanorods during a 48 h hydrothermal treatment at 180 °C with pH value of 4.5–6.0. The obtained nanorods had average diameters of 20 nm and lengths close to 100 nm along [001] direction. Besides the direct precipitation combining hydrothermal treatment, introducing chelating agent is also a powerful tool to restrict crystal growth, regulate the crystallization and get anisotropic materials. Yan et al. firstly used EDTA-assisted hydrothermal method to prepare *t*-$LaVO_4$ nanorods. The transformation from monoclinic phase to the metastable tetragonal structure dramatically enhanced the luminescence intensity of $LaVO_4$:Eu, validating the

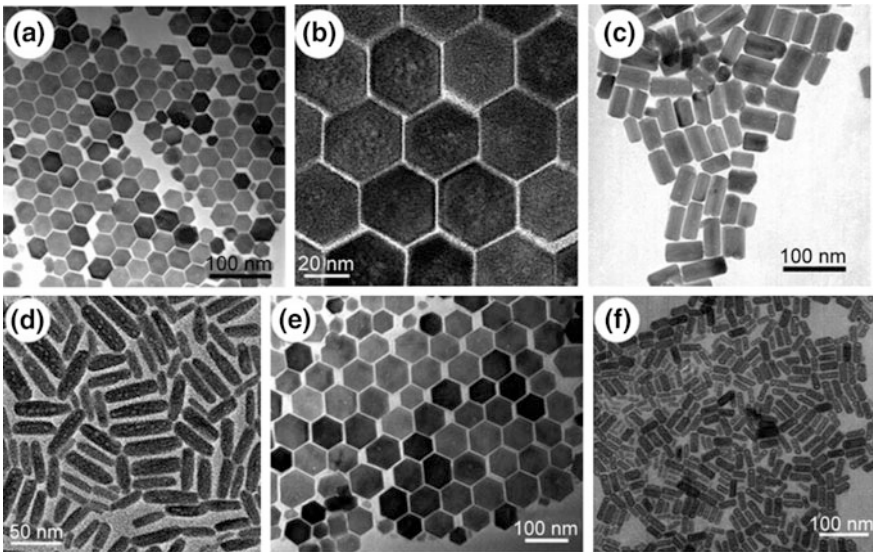

Fig. 5.9 TEM image of $REPO_4 \cdot nH_2O$ nanocrystals: **a** Dy, **b** Er, **c** Ho, **d** Tm, **e** Yb, and **f** Lu. (Reprinted with permission from [57]. Copyright 2007 Wiley-VCH)

correlation between structure and properties of materials [61]. They subsequently found that weak coordinating ligands, like sodium acetate or sodium citrate, only promote the crystallization of *m*-$LaVO_4$, also benefits the homogeneous doping of other rare earth ions in $LaVO_4$ lattice [61], but have no effect on the polymorph selection for the tetragonal phase. Also, by varying the ratio of [EDTA]/[La^{3+}], the aspect ratio of the $LaVO_4$ nanorods/nanowires also could be tuned (as shown in Fig. 5.10) [62, 63]. Employing a reverse microemulsion system with SDS (sodium dodecylsulfate) as the surfactant, Fan et al. obtained *t*-$LaVO_4$ nanowires and nanotubes after 170 °C treatment [64]. By altering the SDS concentration, the morphology of $LaVO_4$ was variable between nanowires and nanorods, and the aspect ratio along the [001] direction could reach 100.

5.2.2 Two-Dimensional (2D) Nanostructures

Recently, 2D nanomaterials, such as nanoplates and nanosheets have attracted broad attention because of their special structures and properties coming from the quantum confinement of electrons [65–68]. However, the facile synthesis of 2D rare earth oxide nanomaterials remains a challenge [69, 70]. Yan's group synthesized a series of dispersible rare earth oxide nanocrystals using rare earth benzoylacetonates [71], acetylacetonates, or acetates [72] as precursors by thermal deposition method

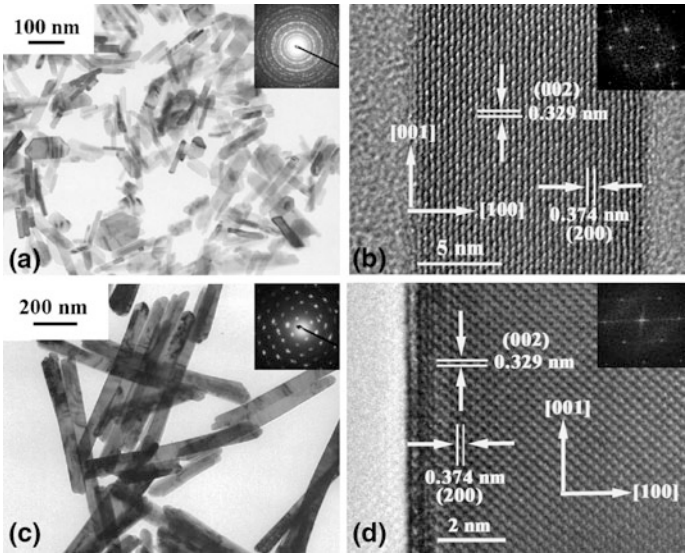

Fig. 5.10 TEM and HRTEM images of as-obtained *t*-$LaVO_4$ nanocrystals (**a** and **b**) and *t*-$LaVO_4$ nanorods (**c** and **d**). (Reprinted with permission from [63]. Copyright 2005 American Association)

(as shown in Fig. 5.11). Interesting, these nanocrystals exhibit a striking ability to self-assemble into large-area nanoarrays. By tuning the polarity of the dispersant, the RE_2O_3 nanocrystals could be aligned to form "side-to-side" or "face-to-face" self-assembly nanoarrays on carbon-coated copper grids [71, 72]. Rare earth oxides with different morphologies, including nanopolyhedra, nanoplates, and nanodisks, were synthesized in oleic acid/oleylamine mixed solvents. The nature of metal cations as well as the selective adsorption of the capping ligands plays a critical role in the shape-controlled growth process.

Murray et al. synthesized ultrathin 2D ceria nanoplates via a thermal decomposition method in the presence of mineralizers (sodium diphosphate) [73]. Many reaction parameters, such as precursor ratio, concentration, and reaction time, were varied to tune the morphology of nanoplates. Sodium diphosphate proved to be critical for accelerating the crystallization process and controlling the morphology of ceria nanocrystals. The obtained CeO_2 nanoplates exhibit much higher oxygen storage capacity than that of 3D CeO_2 nanomaterials prepared with other methods due to their higher theoretical surface-area-to-volume ratio and desirable (100) surfaces.

Generally, metal oxides with a cubic crystal structure, including ceria, inherently do not show any preference for 2D anisotropic growth behaviors. However, Xia et al. prepared ultrathin, single-crystalline ceria nanosheets with a thickness of approximately 2.2 nm and lateral dimension up to 4 μm by a simple aqueous route (as shown in Fig. 5.12) [74]. A balance of the anisotropic hydrophobic attraction and the electrostatic interactions may govern the spontaneous 2D self-organization

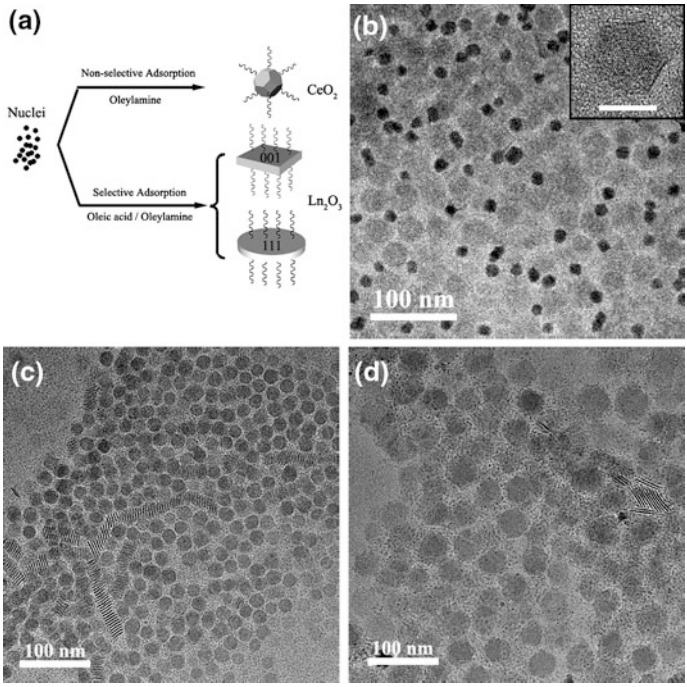

Fig. 5.11 **a** Formation of rare earth oxide nanopolyhedra, nanoplates, and nanodisks. **b–d** TEM images of the as-obtained Eu_2O_3: **b** OA/OM = 1:7, 310 °C, 1 h (*inset* HRTEM image of an Eu_2O_3 nanoparticle; *scale bar* 10 nm); **c** OA/OM = 3:5, 310 °C, 20 min; **d** OA/OM = 3:5, 330 °C, 1 h. (Reprinted with permission from [71]. Copyright 2005 John Wiley and Sons)

of initially formed small ceria nanocrystals. Subsequently, the nanosheets were formed through a recrystallization process. Due to the quantum size effect associated with the extremely small thickness, these ceria nanosheets hold great potentials for fundamental studies.

In order to study the role of active sites in catalysis, Xie's group successfully synthesized three-atom-layer thin CeO_2 sheets with about 20 % pits occupancy using an "ultrafast open space transformation" strategy [75]. An intermediate of ultrathin $CeCO_3OH$ sheets with thin 2D structures were obtained using sodium oleate, $CeCl_3$ and $NH_3 \cdot H_2O$ as the starting materials. Subsequently, freestanding ultrathin CeO_2 sheets with numerous surface pits were synthesized after direct heating of the $CeCO_3OH$ intermediate at 400 °C for 2 min in air. By contrast, they prepared clean three-atom-thick CeO_2 sheets without surface pits by elevating the heating temperature to 550 °C and shortening the duration to 10 s.

Rare earth fluorides and complex fluorides often take 2D shapes. Li et al. synthesized uniform LaF_3 nanoplates with Yb^{3+}/Er^{3+} and Yb^{3+}/Ho^{3+} dopants in a hydrothermal autoclave [76]. Yan's group employed the thermolysis approach with the single precursor $La(CFCOO)_3$ and obtained highly monodisperse LaF_3

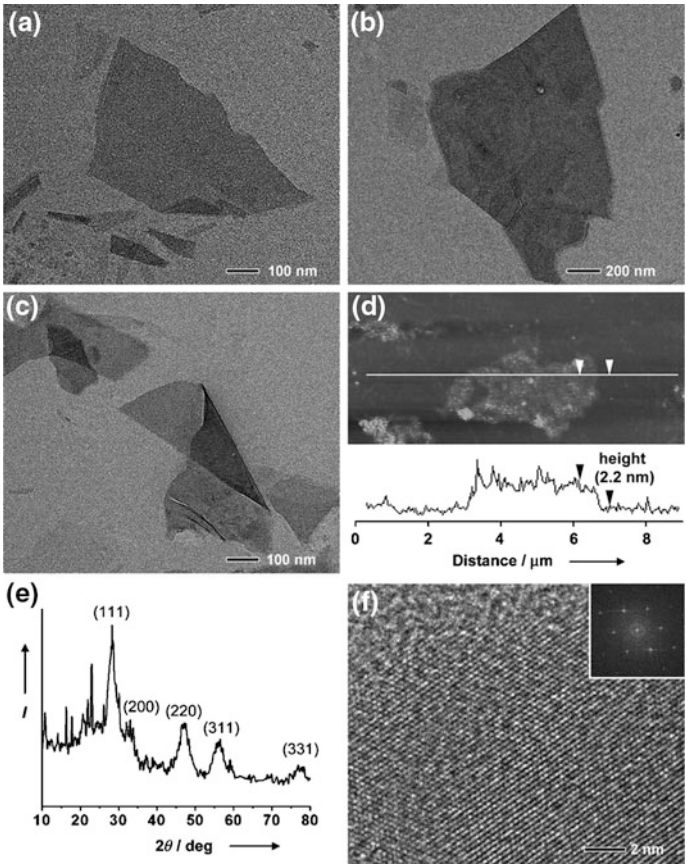

Fig. 5.12 Characterization of ceria nanosheets. **a**, **b** TEM images of nanosheets with different sizes. **c** TEM image of a self-folded nanosheet. **d** Tapping-mode AFM image and the height along the *line* shown in the AFM image. **e** Powder XRD pattern. **f** HRTEM image and the corresponding FT pattern (*inset*). (Reprinted with permission from [74]. Copyright 2010 John Wiley and Sons)

triangular nanoplates [77]. By altering the solvent, the nanoplates can self-assemble into highly ordered superlattices on substrates in a side-by-side or face-to-face manner (as shown in Fig. 5.13). They subsequently obtained monodisperse ultrathin LaOCl nanoplates (*ca.* 4.0 nm in thickness) using a similar method [78], and found that when different long chain amines (oleylamine, hexadecylamine and octadecylamine) were used as the surfactant, the LaOCl nanoplates could self-organize into face-to face and side-by-side superstructures, nanowire-like and nanorod-like superstructures. The different interaction strengths of amine capping ligands were presumed to be responsible for the different behaviors in self-assembly configurations. Apart from self-assembly, the same group also employed Langmuir-Blodgett technique to fabricate dense monolayers of a variety of differently shaped hydrophobic nanostructures [79], including sphere-like $NaYF_4$ and $LiYF_4$ polyhedra, 1D

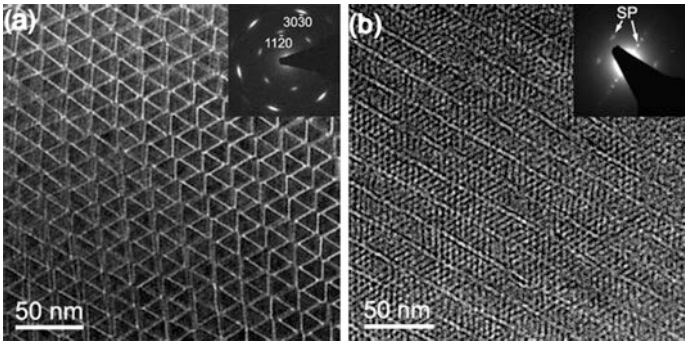

Fig. 5.13 TEM images of the **a** side-by-side and **b** face-to-face superlattices of LaF_3 nanoplates. Insets are the SAED patterns. (Reprinted with permission from [77]. Copyright 2005 American Chemical Society)

$NaYF_4$ nanorods, 2D LaF_3 triangular nanoplates, CaF_2 square nanoplates and EuF_3 hexagonal nanoplates. The effects of size, shape symmetry on the assembly kinetics were discussed.

Examples of 2D rare earth phosphates and vanadates are relatively rare, since they usually take rod-like or spindle-like shapes due to their crystal structures. Li et al. reported an oleic-acid-assisted solvothermal routes in mixed solution of water and ethanol for the synthesis of uniform $REPO_4 \cdot nH_2O$ nanocrystals at 140 ºC [57]. Hexagonal nanoplates with sub-100 nm diagonal diameter could be obtained, which self-assembled on substrate into ordered hexagonal monolayers. Qian et al. synthesized a series of rare earth vanadates and compared the effect of different chelating ligands including trisodium citrate, sodium tartrate and sodium malate [80]. They found when the amount of citrate or tartrate was higher than twofold molar ratio of Y^{3+}, a preferential growth would arise, yielding YVO_4 nanoplates with a donut-like morphology (as shown in Fig. 5.14). This method can be extended to vanadates of heavy lanthanide elements, such as $DyVO_4$ and $ErVO_4$. Li et al. prepared $LaVO_4$:Eu square nanoplates using a hydrothermal method with the assistance of oleic acid as surfactant [81]. The monodisperse 40 nm × 40 nm × 10 nm nanoplates tend to self-organize into ordered 2D arrays. They also synthesized a series of *t*-$REVO_4$ colloidal nanocrystals by using the same method [82]. They found the preferential growth direction of nanocrystals was decided by the steric repulsions of active points on crystal facets. $LaVO_4$, $CeVO_4$, and $PrVO_4$ nanocrystals revealed a square sheet-like morphology since their [100] and [010] directions had smaller rejection. With reducing ionic radius, YVO_4, $NdVO_4$, $SmVO_4$, and $EuVO_4$ showed similar square morphology, but the corners and edges of the nanoplates were broken or damaged. From $EuVO_4$ to $LuVO_4$, the breakage on nanocrystals edges became more pronounced and the proportion of irregular nanocrystals gradually increased. For $TmVO_4$ and $LuVO_4$, the selectivity of crystalline growth direction almost disappeared.

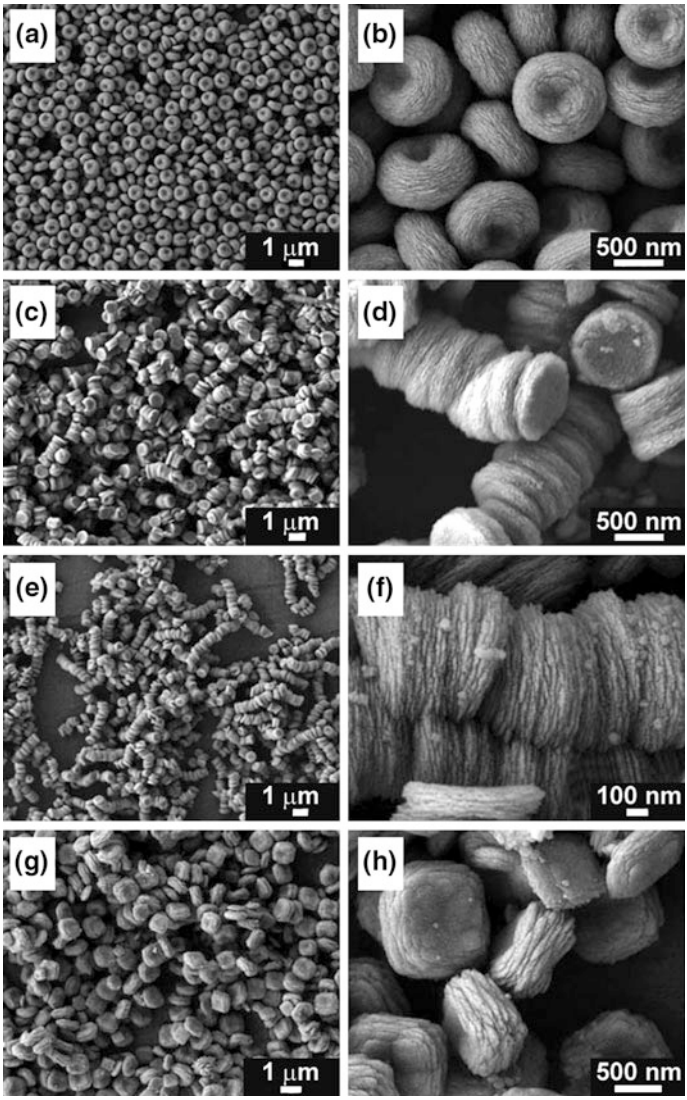

Fig. 5.14 SEM images of monodisperse YVO_4 assemblies obtained from 24 h hydrothermal reaction at 140 °C. Different chelating agents were used. **a**, **b** 2:1 molar ratio of citrate/Y^{3+}; **c**, **d**, 3:1 molar ratio of citrate/Y^{3+}; **e**, **f**, 4:1 molar ratio of citrate/Y^{3+}; **g**, **h**, 2:1 molar ratio of tarate/Y^{3+}. (Reprinted with permission from [80]. Copyright 2009 Wiley-VCH)

5.3 Applications of Rare Earth Based Anisotropic Nanomaterials

5.3.1 Luminescence Properties and Optical Applications

5.3.1.1 General Introduction of the Luminescence Properties of Rare Earths

Featuring abundant energy levels of 4f electron configurations, trivalent rare earth ions activated nanocrystals exhibit unique and fascinating luminescence properties [83]. Compared with semiconductor quantum dots and organic dyes, rare earth activated nanocrystals possess excellent photostability, large Stokes/anti-Stokes shifts, sharp-band emissions, and long luminescence lifetimes [84]. Benefiting from these advantages, RE-activated nanocrystals are promising candidates for applications in lighting and displays [85], optical fibers and amplifiers [86], bioimaging [87], photoactivation reactions [88], and photovoltaic devices [89].

With differently arranged energy levels, various rare earth activators are endowed with distinctive transition pathways. Ce^{3+}, widely studied and used for phosphor activators, is featured by its broadband 4f → 5d transition [90]. For other RE^{3+} activators, intra-configurational 4f → 4f transitions are the main intrinsic mechanism for their luminescence processes. Three different pathways for intra-configurational transition may occur in rare earth ions, namely, down-shifting, quantum-cutting (also known as downconversion), and upconversion (as shown in Fig. 5.15). In a down-shifting process, a high-energy excitation photon results in a low-energy one emitted, with the quantum efficiency below 100 %. Tb^{3+}, Eu^{3+}, Sm^{3+} and Dy^{3+} are typical activators for the down-shifting studies [91]. Due to their sufficiently high efficiencies and long luminescence lifetimes, down-shifting-based nanocrystals have been employed as candidates for lighting and displays and

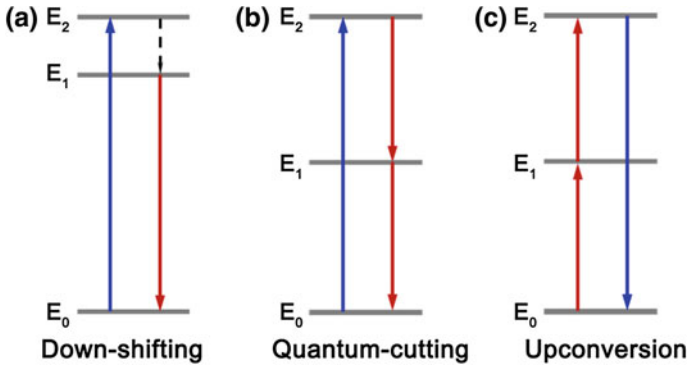

Fig. 5.15 Simplified illustration of intra-configurational transition pathways for rare earth ions. **a** Down-shifting. **b** Quantum-cutting (or downconversion). **c** Upconversion. The *upward*, *downward* and *dashed arrows* represent excitation, emission and relaxation processes, respectively

time-resolved biodetection applications [92, 93]. In a quantum-cutting process, one high-energy excitation photon splits into two (or more) low-energy ones by cascading down the ladder-like energy levels, with the quantum efficiency above 100 %. Nanocrystals with Pr^{3+}/Gd^{3+}–RE^{3+} (RE = Eu, Tb, Er) pairs and Yb^{3+}–RE^{3+} (RE = Tb, Tm, Pr) pairs dominate the quantum-cutting studies [94]. Considering the high quantum efficiency and specific visible or near-infrared (NIR) emissions, quantum-cutting-based nanocrystals are promising in lighting, displays, and particularly, improvement for solar cells [95, 96]. The photon upconversion process refers to a non-linear optical process where two (or more) low-energy excitation photons generate a high-energy one assisted by real intermediate excited states, with the quantum efficiency below 100 % [97]. In this section, we will mainly discuss the photon upconversion processes and extended optical applications of rare earth activated anisotropic nanocrystals.

5.3.1.2 Photon Upconversion in Rare Earth Anisotropic Nanostructures

Due to the high conversion efficiency, energy transfer upconversion (ETU) emissions have been widely studied. Two different types of luminescent centers, namely, a sensitizer and an activator, are involved in the ETU process [98–100]. Yb^{3+}, with only one excited state ($^2F_{5/2}$) and a large absorption cross-section at 980 nm, is an outstanding sensitizer for the ETU process. Moreover, the energy of $^2F_{5/2}$ state matches well with that of most rare earth ions, which also facilitates Yb^{3+} as a commendable sensitizer. With ladder-like arranged energy levels, long-lived intermediate excited states and excellent resonance with the energy gap from $^2F_{7/2}$ to $^2F_{5/2}$ of Yb^{3+}, Er^{3+}, Tm^{3+}, and Ho^{3+} (especially Er^{3+} and Tm^{3+}) ions are ideal pairing activators for the ETU process. In addition, the host matrices also have significant influences on the upconversion behaviors of doped luminescent centers. Generally, rare earth based fluorides and complex fluoride salts are considered as optimal host matrices due to their low phonon energy and high transparency for NIR photons [101–103].

In Yb^{3+}–Er^{3+} activated nanocrystals, three-photon 415 nm emission ($^2H_{9/2} \rightarrow {}^4I_{15/2}$), two-photon 525, 545 and 655 nm emissions ($^2H_{11/2} \rightarrow {}^4I_{15/2}$, $^4S_{3/2} \rightarrow {}^4I_{15/2}$, $^4F_{9/2} \rightarrow {}^4I_{15/2}$) can be observed after the successive energy transfer from Yb^{3+} to Er^{3+} (Fig. 5.16a) [104]. In Yb^{3+}–Ho^{3+} activated nanocrystals, three-photon 485 nm emission ($^5F_3 \rightarrow {}^5I_8$), two-photon 545 nm emission ($^5F_4$, $^5S_2 \rightarrow {}^5I_8$) and 650 nm emission ($^5F_5 \rightarrow {}^5I_8$) are the typical upconversion spectral fingerprints (Fig. 5.16b) [105]. The densely arranged energy levels of Er^{3+} and Ho^{3+} determine that multiple photon upconversion processes are scarcely observed in Yb^{3+}–Er^{3+} and Yb^{3+}–Ho^{3+} activated nanocrystals. However, multiple photon upconversion emissions, coming from three-, four-, and five-photon transitions, can be frequently detected in Yb^{3+}–Tm^{3+} activated nanocrystals. This should be attributed to the discretely arranged energy levels of Tm^{3+}, which, to a large extent, reduce the non-radiative relaxation processes. Therefore, two-photon 800 and 695 nm emissions

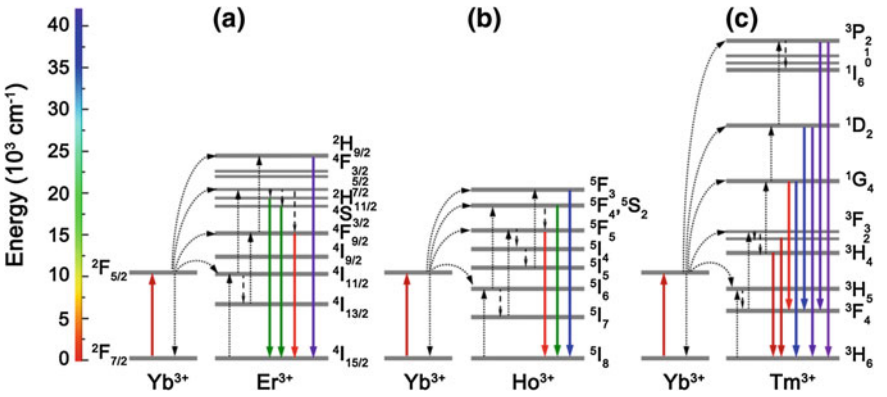

Fig. 5.16 Proposed upconversion energy transfer pathways in **a** Yb^{3+}–Er^{3+}, **b** Yb^{3+}–Ho^{3+} and **c** Yb^{3+}–Tm^{3+} pairs. Excitation and emission processes are represented by *upward* and *downward solid arrows*, respectively. The *dotted* and *dashed arrows* denote energy transfer and non-radiative relaxation processes, respectively

($^3H_4 \rightarrow {}^3H_6$, $^3F_3 \rightarrow {}^3H_6$), three-photon 645 and 475 nm emissions ($^1G_4 \rightarrow {}^3F_4$, $^1G_4 \rightarrow {}^3H_6$), four-photon 450 and 365 nm emissions ($^1D_2 \rightarrow {}^3F_4$, $^1D_2 \rightarrow {}^3H_6$), and even five-photon 345 and 290 nm emissions ($^1I_6 \rightarrow {}^3F_4$, $^1I_6 \rightarrow {}^3H_6$) can be simultaneously released from Yb^{3+}–Tm^{3+} pairs (Fig. 5.16c) [106].

When rare earth activated nanocrystals adopt anisotropic morphologies, their upconversion properties differ greatly from those with isotropic ones, especially the polarized upconversion emissions. Qiu et al. for the first time investigated the polarized upconversion emissions from Yb^{3+}–Tm^{3+} activated hexagonal phased $NaYF_4$ single nanorod [107]. Upon excitation with a 980 nm linearly polarized laser, sharp energy level splitting of the $^1D_2$ and $^1G_4$ states of Tm^{3+} was observed at room temperature, generating singlet-to-triplet emissions at 735 nm ($^1D_2 \rightarrow {}^3F_3$) and 768 nm ($^1G_4 \rightarrow {}^3H_5$), which previously were assumed to be partially forbidden (Fig. 5.17a). In the meanwhile, the multiple discrete emission intensity periodic variation with polarized direction was also observed (Fig. 5.17b). Moreover, the aspect ratio of nanorod was studied for the effect on the polarization property (Fig. 5.17c). Hexagonal-phased $NaYF_4$:Yb,Tm single nanorod and single nanodisk were found to possess quite similar fitting contours in each transition of Tm^{3+}, suggesting a negligible effect of aspect ratio on the polarization anisotropy. However, when Gd^{3+} ions were doped into the nanorods, the polarization anisotropy became distinctly different. Two different kinds of intensity variation states were observed for each transition. The authors reasoned that the different local symmetry of Tm^{3+} in $NaYF_4$:Gd,Yb,Tm nanorods should be responsible. Based on the comprehensive studies, the intrinsic transition properties and crystal local symmetry should dominate the polarization anisotropy.

Apart from the polarization anisotropy, the pleochroism of upconversion emissions is also embodied in anisotropic nanocrystals. Yan et al. prepared a series of hexagonal phased $NaYF_4$:Yb,Er nanocrystals with different sizes ranging from

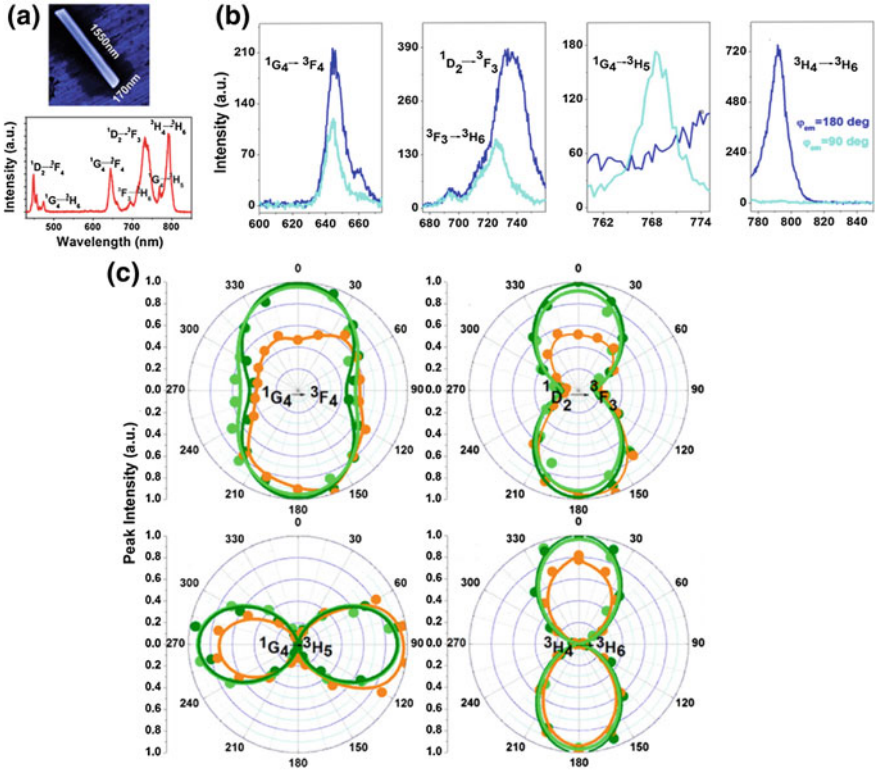

Fig. 5.17 **a** Scanning electron microscopy image of $NaYF_4$:Yb,Er nanorod and its upconversion emission spectrum upon excitation with a 980 nm linearly polarized laser. **b** Polarization angle (φ_{em}) dependent upconversion emission spectra. **c** Polar plots of the upconversion peak intensity as a function of the emission polarization angle, which is corresponding to the transitions of Tm^{3+} in $NaYF_4$:Yb,Er nanorod, nanodisk, and $NaYF_4$:Gd,Yb,Er nanorod. (Reprinted with permission from [107]. Copyright 2013 American Chemical Society)

$\sim$20 to $\sim$300 nm. As the size increased, the morphology of the nanocrystals changed from spherical to disk-like. And the green-to-red emission ratio of Er^{3+} was found to increase with the nanocrystals from isotropic to anisotropic (Fig. 5.18) [104, 108]. Furthermore, the authors investigated the upconversion behavior of one-dimensional $NaMgF_3$:Yb,Er nanorods. Different from the upconversion profile of hexagonal-phased $NaYF_4$:Yb,Er nanodisks, for which the green emission dominated the visible regime, the green emission from $NaMgF_3$:Yb,Er nanorods was significantly weaker than the red emission [109]. Recently, they developed a novel structure of $NaYF_4$:Yb,Er nanocages, deriving from the removal of NaCl in NaCl/$NaYF_4$:Yb,Er core/cage nanocomposites. The upconversion behavior of $NaYF_4$:Yb,Er nanocages and nanospheres were examined. It was found that the red-to-green emission ratio of Er^{3+} decreased to 0.44 in nanocages from 1.89 in nanospheres [110]. Zhu et al. compared the upconversion profiles of orthorhombic

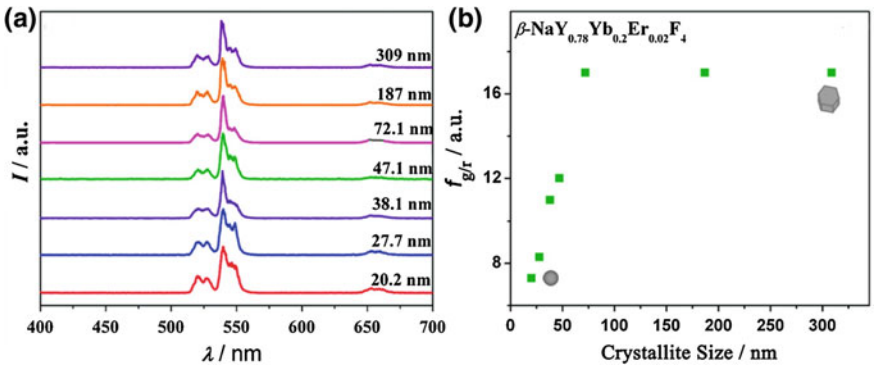

Fig. 5.18 **a** Upconversion emission spectra of different sized hexagonal $NaYF_4$:Yb,Er nanocrystals in cyclohexane. **b** Diagram of *green* to *red* emission ratio versus the size of $NaYF_4$:Yb,Er nanocrystals, with *insets* representing the morphology transition from isotropic to anisotropic. (Reprinted with permission from [104]. Copyright 2007 American Chemical Society)

KSc_2F_7:Yb,Er nanorods with hexagonal $NaYF_4$:Yb,Er nanorods [111]. They observed greatly enhanced red and violet emissions of Er^{3+} in KSc_2F_7:Yb,Er nanorods. Liu et al. prepared 1D orthorhombic KYb_2F_7:Yb,Er nanorods, where Yb^{3+} ions were localized as tetrad clusters. The spectral results exhibited that multiphoton violet emission of Er^{3+} was significantly enhanced compared with that in hexagonal $NaYF_4$ nanodisks [112]. Moreover, the violet emission of Er^{3+} was assigned as a four-photon emission.

When multiple activators are embedded in anisotropic nanocrystals, the upconversion emissions become more intriguing. Li et al. studied the upconversion behavior of hexagonal phased $NaYF_4$:Yb,Ho nanorods after Ce^{3+} doping [113]. They observed that the red-to-green emission ratio of Ho^{3+} increased after the introduction of Ce^{3+}, with the emission output from pure green to greenish-yellow. Moreover, unusual $^5G_5 \rightarrow {}^5I_7$ and $^5F_2$, $^3K_8 \rightarrow {}^5I_7$ transitions of Ho^{3+} and 5d → 4f transitions of Ce^{3+} can be simultaneously observed. Qin et al. modulated the red-to-green emission ratio of Er^{3+} in hexagonal-phased $NaYF_4$ one-dimensional microtubes by precisely defining the doping ratio of Tm^{3+} dopant [114]. An increased red-to-green emission ratio of Er^{3+} was detected with elevated content of Tm^{3+} from 0 to 2 mol%, with the emission output altering from green to red. Multiphoton cross-relaxations within Tm^{3+}–Er^{3+} pairs were proposed to account for the spectral variation. Lee et al. fabricated a series of quasi-two-dimensional anisotropic core/shell nanostructures, where the shell layers preferentially grew on the side faces (100) of the hexagonal phased $NaYF_4$ nanocrystals. Er^{3+} and Tm^{3+} ions were separately embedded in the core and shell regions, respectively, giving out multicolor upconversion emissions upon NIR excitation [115]. Recently, Liu et al. employed an end-on growth of upconversion nanocrystals compromising Tm^{3+} and Er^{3+} ions onto the hexagonal one-dimensional $NaYF_4$ nanorods. The emission output was further modulated by tuning the molar ratio of sensitizer and activator.

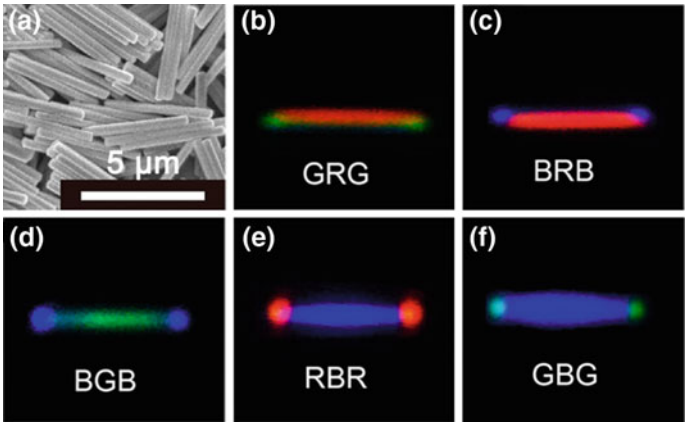

Fig. 5.19 **a** Scanning electron microscopy image of $NaYF_4$ based nanorod. **b–f** Optical micrographs showing five sets of dual-color-banded upconversion nanorods. Note that the appearance of a tinge color at the tip junction is due to the chromatic aberration and limited resolution of the microscope. (Reprinted with permission from [116]. Copyright 2014 American Chemical Society)

A series of dual-color upconversion nanorods displaying different combinations of the three primary colors were obtained (Fig. 5.19). With the dual-color emitting nanorods, they achieved some prototype models for barcoding for anti-counterfeiting application [116].

Recent progresses show that upconversion emissions from anisotropic nanocrystals can be tailored by the other co-assembled nanomaterials. Yan et al. investigated the upconversion emissions from a two-dimensional dense film of $NaYF_4$:Yb,Er nanocrystals by co-assembling with Ag nanowires [117]. They noticed 2.3 fold and 3.7 fold enhancement for the green and red emissions, respectively. And the large scattering efficiency of Ag nanowires was proposed to account for the enhancement. Kagan et al. studied the upconversion emission in an assembly comprising single $NaYF_4$:Yb,Er nanodisk and single Au nanorod (as shown in Fig. 5.20) [118]. The longitudinal surface plasmon resonance of the Au rod was tuned to match the 977 nm excitation wavelength of the $NaYF_4$:Yb,Er nanodisk by tailoring the dimension of the rod. And the spatial distance between the two composites was within the range of the intense near-fields surrounding the Au rod tips. As a result, two and threefold enhancements were achieved for the green and red emissions of Er^{3+}, respectively. Moreover, the enhancements exhibited a strong dependence on the polarization of the excitation light relative to the Au rod axis. The longitudinal polarization exhibited more spectral changes than the transverse one. Zink et al. encapsulated single $NaYF_4$:Yb,Er nanorod and single smaller superparamagnetic Fe_3O_4 nanocrystal into one mesoporous silica nanoparticle, and further exposed the nanocomposites to oscillating magnetic field [119]. The upconversion behavior of $NaYF_4$:Yb,Er nanorod was modulated by heat magnetically induced by Fe_3O_4 inside the nanocomposites. Spectral results showed

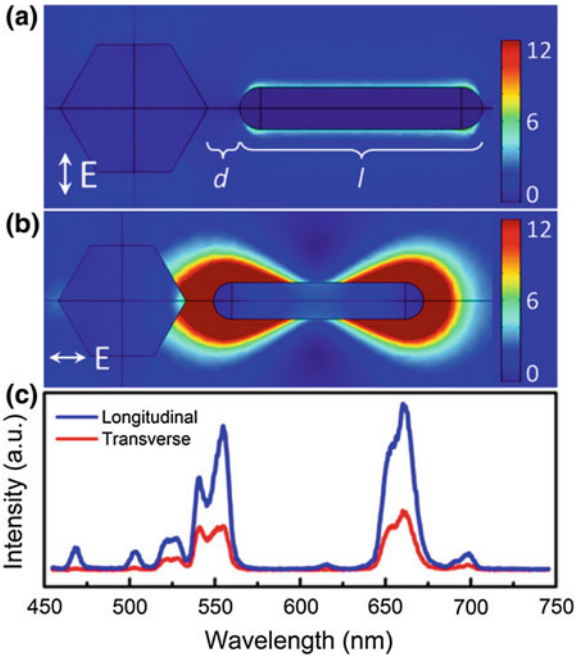

Fig. 5.20 Simulated field intensity enhancement maps for **a** transverse and **b** longitudinal excitation polarization. **c** Representative upconversion emission spectra from the center of the $NaYF_4$:Yb,Er nanodisk under longitudinal (*blue*) and transverse (*red*) incident polarization for the Au–$NaYF_4$:Yb,Er assembly. (Reprinted with permission from [118]. Copyright 2014 American Chemical Society)

that the emission ratio of 525 to 545 nm of Er^{3+} enhanced with elevated temperature, which resulted from prolonged exposure time to the magnetic field.

The excitation pathways can be modulated in anisotropic nanocrystals as well. Yan et al. extended the NIR excitation band of Yb^{3+}–RE^{3+} (RE = Er, Tm) pairs by introducing Nd^{3+} into a separated layer with an array of Yb^{3+} ions as the energy bridgers (Fig. 5.21) [120]. As a result, almost similarly efficient upconversion emissions can be obtained upon 980 nm (for Yb^{3+}) and 808 nm (for Nd^{3+}) excitations. Moreover, the potential overheating issue induced by longtime 980 nm irradiation was largely minimized by shifting the excitation wavelength to 808 nm. Similarly, Wang et al. also realized energy transfer management in multishell structured anisotropic nanorods upon 808 nm excitation [121]. Besides spatial separation of Nd^{3+} and activators, Han [122] and Liu [123] also achieved cascade sensitization of upconversion emissions by co-doping Nd^{3+} and Er^{3+}/Tm^{3+} in the same layer.

5.3.1.3 Optical Applications

The past few years witnessed the rapid development of rare earth upconversion nanocrystals in various aspects, including bioimaging studies [124], theranostics [125], sensing and detection [126], photovoltaic devices [127], and photoactivation

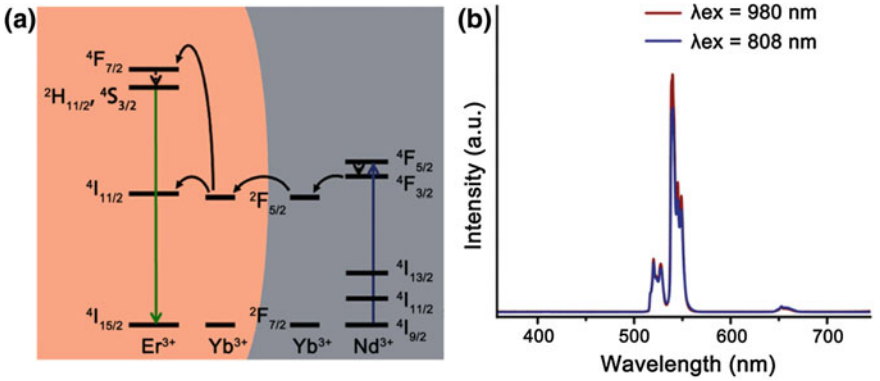

Fig. 5.21 **a** Proposed energy transfer pathways for Nd^{3+} activated upconversion emissions. **b** Typical upconversion emission spectra of Yb^{3+}–Er^{3+} activated nanocrystals upon 980 and 808 nm excitations. (Reprinted with permission from [120]. Copyright 2013 American Chemical Society)

reactions [128]. In this part, we will present a brief summary of rare earth upconversion nanocrystals for applications in biology and photoresponsive materials.

Due to the specific NIR excitation, resolvable UV to NIR emission and deep tissue penetration, rare earth upconversion nanocrystals have been widely used as biomarkers for biological studies. Various models, such as cells [129], *C. elegans* [130], rats [131] and rabbits [132], have been employed to assess the bioimaging performance of rare earth upconversion nanocrystals. Yan et al. examined the bioimaging capability and assessed the toxicity of $NaYF_4$:Yb,Tm nanocrystals in vitro and in vivo [133]. After incubation with the upconversion nanocrystals, bright upconversion emission signals can be collected from HeLa cells and *C. elegans* (Fig. 5.22). Moreover, no obvious toxicity effect was found for both cells and *C. elegans*. Li et al. synthesized sub-10 nm hexagonal $NaLuF_4$:Gd,Yb,Er nanocrystals and applied them for sensitive in vivo imaging. Subcutaneous imaging of 50 KB cells and intramouse imaging of 1000 KB cells after intravenous injection were obtained [134].

Besides single-modal optical imaging, rare earth upconversion nanocrystals have also been assembled with magnetic nanocrystals, noble metal nanocrystals and photosensitive molecules to support multi-modal imaging, theranostic and biodetection applications. Liu et al. deposited Au and Fe_3O_4 nanocrystals onto hexagonal $NaYF_4$:Yb,Er nanodisks to conduct photothermal therapy, magnetic resonance imaging and upconversion imaging studies [135]. Yan et al. fabricated multifunctional $NaGdF_4$:Yb,Er@CaF_2@SiO_2 nanocomposites, which were further grafted with photosensitizers to generate singlet oxygen, for upconversion imaging, magnetic resonance imaging and photodynamic therapy [136]. Li et al. decorated NIR cyanine dye hCy7 molecules on hexagonal $NaYF_4$:Yb,Er,Tm nanocrystals. When $MeHg^+$ ions were added to the nanocomposites, the red emission of Er^{3+} became significantly enhanced while the NIR emission of Tm^{3+} sharply decreased.

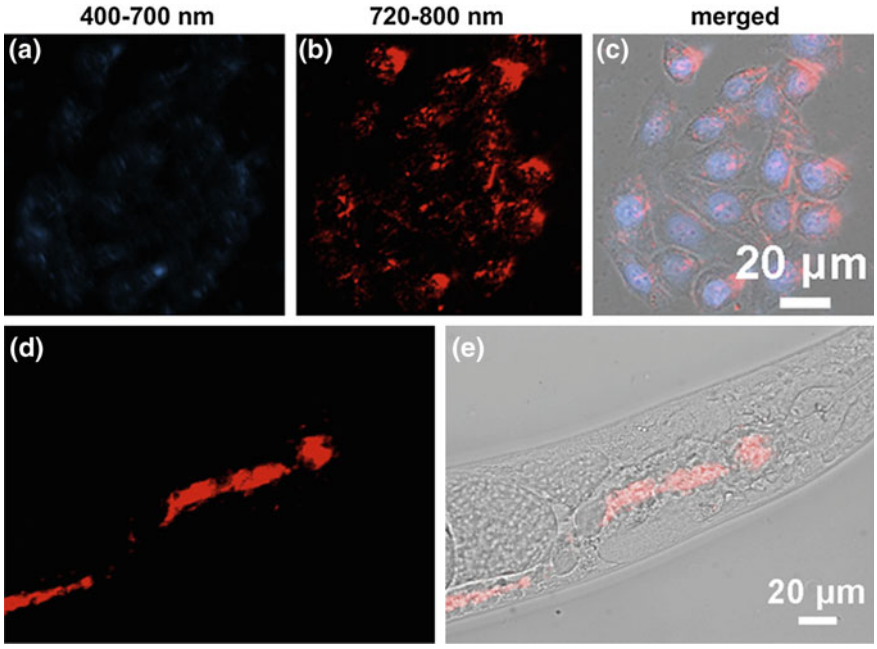

Fig. 5.22 In vitro and in vivo bioimaging of $NaYF_4$:Yb,Tm nanocrystals. **a**, **b** False-colored upconversion emission signals in visible (400–700 nm) and NIR (720–800 nm). **c** Merged images of HeLa cells and upconversion emissions. **d**, **e** False-colored NIR upconversion emission signal and the merged image of *C. elegans*. (Reprinted with permission from [133]. Copyright 2011 Elsevier B.V.)

They realized both in vitro and in vivo detection of $MeHg^+$ ions with the detection limit of 0.18 ppb [137].

Upconversion emissions from rare earth activated nanocrystals are also demonstrated to trigger photoactivation reactions. Diarylethene derivatives, *o*-nitrobenzyl containing molecules, and azobenzenes are typical photoresponsive molecules. Branda et al. used alternative irradiation of upconversion emissions from $NaYF_4$:Yb, Tm and $NaYF_4$:Yb,Er nanocrystals to remotely control the photoswitching process of diarylethene derivatives [138]. By precisely defining the composition of upconversion nanocrystals and tuning the NIR excitation power, reversible photoswitching process of diarylethene derivatives was achieved [139]. Xing et al. reported a novel type of nanocomposites for controllable release of D-luciferin molecules, which were decorated on the surface of $NaYF_4$:Yb,Tm nanocrystals via the *o*-nitrobenzyl group. Upon NIR excitation, UV emissions from Tm^{3+} can trigger the disassociation of D-luciferin molecules [140]. Recently, Yan and Li et al. fabricated a NIR-light-responsive self-organized helical superstructure by doping chiral azobenzenes and two-dimensional (2D) Yb^{3+}–Tm^{3+} activated nanodisks into a liquid crystal host. Upon high power excitation, UV emissions (Fig. 5.23a) from Tm^{3+} can direct the

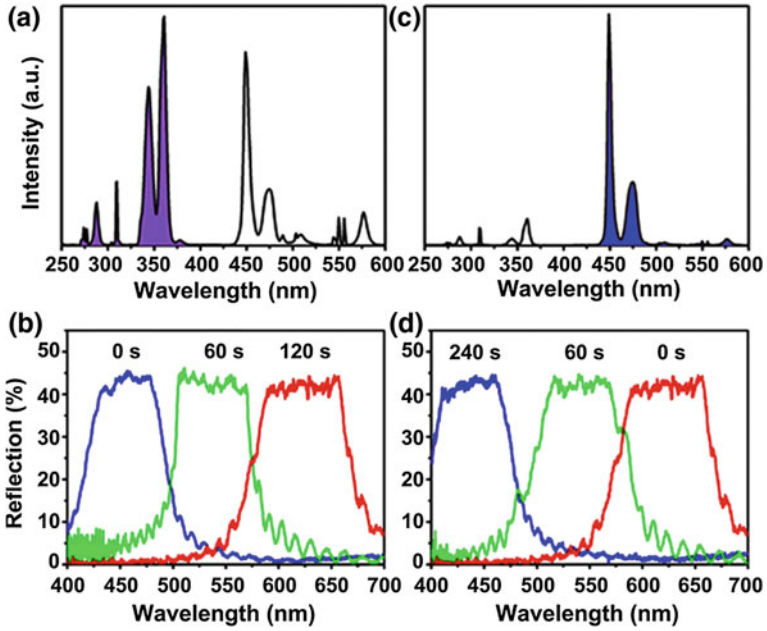

Fig. 5.23 Upconversion emission spectra from Yb^{3+}–Tm^{3+} activated nanodisks and reflection spectra of liquid crystal upon high power excitation (**a**, **b**) and low power excitation (**c**, **d**). (Reprinted with permission from [141]. Copyright 2014 American Chemical Society)

trans to *cis* isomerization of azobenzenes, resulting a red-shifted reflection wavelength of the liquid crystal (Fig. 5.23b). At low power excitation, the blue emissions (Fig. 5.23c) from Tm^{3+} are observed to trigger the reversible process of the blue-shifted absorption of liquid crystal (Fig. 5.23d) [141].

5.3.2 Magnetic Properties and MRI Applications of Anisotropic Rare Earth Nanostructures

The rare earth elements are well known for their superior magnetic properties. Their trivalent ions are characterized by f^n configurations, which renders them large paramagnetic susceptibility (expect Sc^{3+}, Y^{3+}, La^{3+} and Lu^{3+}, due to their lack of 4f unpaired electrons) [142]. Different from the 3d electrons of some transition metal ions (Fe^{3+}, Mn^{2+} and Co^{2+}, etc.), the 4f electrons of rare earth ions are less influenced by the microenvironment, as they are shielded by outer-shell ($5s^25p^6$) electrons. Besides, some of their compounds possess distinctive magnetic properties, such as large saturation magnetization, large magnetocrystalline anisotropy constant, large magnetostriction constant and remarkable magneto-optic effect [143]. As a result, rare earth materials have been widely used in traditional magnet

Table 5.1 Ground state, g values, calculated and experimental room temperature χT value for Ln (III) ions

Ln (III)	Configuration	Ground state	g_J	χT^{a}_{cal} (emu mol^{-1} K)	χT_{exp} (emu mol^{-1} K)
Ce	f^1	$^2F_{5/2}$	6/7	0.8	0.66–0.78
Pr	f^2	$^3H_4$	4/5	1.6	1.45–1.62
Nd	f^3	$^4I_{9/2}$	8/11	1.64	1.45–1.53
Pm	f^4	$^5I_4$	3/5	0.9	1.05
Sm	f^5	$^6H_{5/2}$	2/7	0.09	0.32
Eu	f^6	$^7F_0$	0	0	1.53
Gd	f^7	$^8S_{7/2}$	2	7.88	7.61–7.8
Tb	f^8	$^7F_6$	3/2	11.82	11.76–12.01
Dy	f^9	$^6H_{15/2}$	4/3	14.17	13.01–14.05
Ho	f^{10}	$^5I_8$	5/4	14.07	13.26–13.78
Er	f^{11}	$^4I_{15/2}$	6/5	11.48	11.05–11.28
Tm	f^{12}	$^3H_6$	7/6	7.15	7.03
Yb	f^{13}	$^2F_{7/2}$	8/7	2.57	2.53

Reprinted with permission from [142]. Copyright 2009 Springer Science and Business Media
[a] $\chi T_{cal} = (1/8)\ g_J^2[J(J+1)]$

technology over the past decades, for example, $SmCo_5$ and $Nd_2Fe_{14}B$ are well-known permanent magnets for their large static magnetic field; yttrium barium copper oxide are famous for displaying high-temperature superconductivity. With the development of nanotechnology, rare earth magnetic materials also have proved their great potential for applications in nanoscale, particularly in the field of magnetic resonance imaging (MRI) (Table 5.1).

As a very powerful noninvasive detection protocol, MRI has superb advantages, such as fast scan time, deep penetration, high spatial resolution, and no radiochemical damage [144, 145]. Nevertheless, the low imaging sensitivity hampered its further application. MRI contrast agents (CAs), which are able to alter the relaxation time of surrounding protons, have been utilized to improve the sensitivity both in clinical diagnosis and biological research [146]. Longitudinal relaxation enhancement is mainly related to the inner-sphere regime that chemically exchanges directly with the paramagnetic centers, while transverse relaxation enhancement is mainly related to proton's effective diffusion and interaction with magnetic dipolar moment in outer-sphere regime (Fig. 5.24) [147]. The ability of CAs to shorten longitudinal relaxation time (T_1) and transverse relaxation time (T_2) is evaluated by longitudinal relaxivity (r_1) and transverse relaxivity (r_2), respectively. Generally, CAs with low r_2 to r_1 ratio (r_2/r_1) are used for T_1-weighted images, while CAs with high r_2/r_1 are used for T_2-weighted images. For clinic, Gd-based chelates (especially Gd-DTPA) and superparamagnetic iron oxide nanoparticles (SPIO) are most widely used T_1 and T_2 CAs, respectively. To lower the risks of free Gd^{3+}, [148] most clinical lanthanide CAs are used in form of chelates, so as to stabilize Gd^{3+} by coordination [149, 150]. However, the leakage of Gd^{3+} is

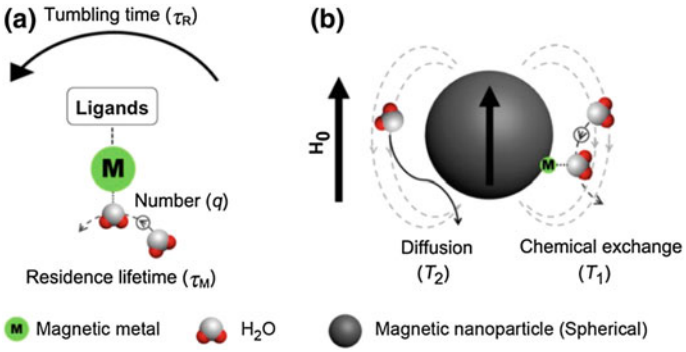

Fig. 5.24 Schematic illustrations of proton phenomena in magnetic systems relating to T_1 and T_2 relaxations. **a** Paramagnetic metal complex system and the selected key parameters to T_1 relaxation of protons: molecular tumbling time (τ_R), proton residence lifetime (τ_M), and the coordinating water molecular number (q), while the magnetic gradient field around paramagnetic center is neglected. **b** Phenomena of proton interaction with a spherical magnetic nanoparticle system: water molecular diffusion and chemical exchange with surface magnetic metals, related to their T_2 and T_1 contrast enhancements, respectively. (Reprinted with permission from [147]. Copyright 2014 American Chemical Society)

inevitable due to coordination equilibrium. Moreover, the Gd^{3+}-based chelates usually have small molecular weight, resulting in rapid clearance from human body. Aiming to solve the present problems of chelate CAs, the concept of nanoparticulate CAs has been raised [151]. The advantages of nanoparticle-based CAs include: (1) rigid inorganic structure could minimize the leakage of Gd^{3+}; (2) high payload of Gd^{3+} per nanoparticle could ensure large local contrast enhancement; (3) larger size than chelates could prolong not only the circulation time in vivo, but also the rotational correlation time (τ_R); (4) multi-functional bio-applications can be realized through doping and further surface engineering.

5.3.2.1 Gd-Based Anisotropic Nanostructures as MRI CAs

With seven unpaired electrons and isotropic orbitals, Gd^{3+} has both large magnetic moment and long electric relaxation time (due to the negligible spin–orbit interaction), and is widely accepted as the best choice for longitudinal proton relaxation enhancement [150]. Nano-sized gadolinium oxide nanoparticles were first evaluated for their physicochemical and NMR properties by McDonald et al. in 2003 [152], which opened the research field of rare earth-based nanoparticulate MRI CAs. Up to now, the studies of Gd-based T_1 CAs have been extended from gadolinium oxides (Gd_2O_3) to gadolinium hydroxide ($Gd(OH)_3$), gadolinium fluoride (GdF_3), sodium gadolinium fluoride ($NaGdF_4$) and gadolinium oxysalts (such as

$GdPO_4$), etc. Besides, doping Gd^{3+} into other inorganic matrices has become an effective strategy to combine MRI with other imaging modalities [153].

Relaxivity is one of the most important indexes for CAs, which could reflect the contrast enhancement efficacy. High relaxivity is always pursued, since it will bring benefits including improved image quality, reduced injection dose and lower risks. However, the r_1 value of Gd-DTPA is quite low (about 4 s^{-1} mM^{-1} at 1.5 T) [154]. Although Gd-based nanoparticles were supposed to have higher relaxivities than Gd-DTPA in the beginning, the r_1 values of those nanoparticles in early stage were still not sufficiently high. This probably could be explained by the immaturity of synthetic methods, since those nanoparticles usually had irregular shapes and wide size distribution. In recent years, with the development of synthetic method, uniform and monodispersed nanoparticles could be readily obtained, and size has been found to significantly affect the relaxivity. Lee et al. synthesized ultrasmall paramagnetic Gd_2O_3 nanoparticles with the size around 1 nm and a large r_1 was estimated (9.9 s^{-1} mM^{-1}) [155]. They discussed the size dependence of r_1 in two terms, surface to volume ratio (*S/V*) and cooperative induction effect. On one hand, it is indicated that only surface Gd^{3+} significantly contribute to the longitudinal relaxation. Therefore, decreasing the size will lead to larger *S/V* and more surface Gd^{3+}, and positively influence the r_1. On the other hand, several surface Gd^{3+} could possibly accelerate the longitudinal relaxation of water protons by cooperative induction. When the size is too small to produce this effect, the r_1 value would decrease. The optimal range of particle size that they suggested is 1–2.5 nm (Fig. 5.25). van Veggel et al. reported on the size-tunable synthesis of $NaGdF_4$ nanoparticles below 10 nm [156]. Through the analysis of the relationship between

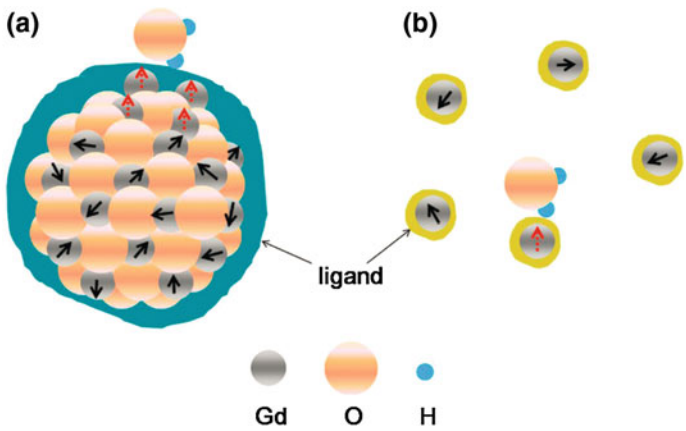

Fig. 5.25 Schematic diagram showing that **a** four surface Gd(III) ions as an example cooperatively induce the longitudinal relaxation of the water proton, whereas **b** such an effect does not exist in individual Gd(III)−chelates. The interacting and non-interacting Gd(III) ions with a water proton are denoted as *dotted* and *solid arrows* for their spins, respectively. The ligands are drawn arbitrarily. (Reprinted with permission from [155]. Copyright 2009 American Chemical Society)

particle size and r_1, they revealed that surface Gd^{3+} are the major contributors to the relaxivity enhancement, and surface Gd^{3+} on a larger nanoparticle affect the relaxivity more strongly than those on a smaller nanoparticle.

Besides *S/V*, τ_R is another important parameter affecting relaxivity, which is mainly determined by hydrated radii of nanoparticles [157]. For 0D nanomaterials, the τ_R value shortens with decreasing size, counteracting the effect of *S/V* towards relaxivity. Whereas for rare earth based nanomaterials with anisotropic morphology, the effect of *S/V* and τ_R could be consistent, as a result, high relaxivity could be realized through rational design of anisotropic nanoparticles.

For 1D nanostructures, most of the Gd-based nanomaterials have rod-like morphology. Suzuki et al. synthesized dextran coated rod-like $GdPO_4$ nanoparticles, with 20–30 nm in the major axis and 6–15 nm in the minor axis [157]. The nanoparticles showed high r_1 and r_2 values of 13.9 and 15.0 s^{-1} mM^{-1}, respectively, and 1.1 as the r_2/r_1 value at 0.47 T. The tumors in rabbit could be effectively visualized with only 1/10 of the applied dose compared to the clinically used Gd-DTPA [158].

Rod-like $Gd(OH)_3$ nanoparticles with the length of 150 nm were synthesized by Gillis et al., showing r_1 and r_2 of 4.03 and 8.0 s^{-1} mM^{-1}, respectively, at 1.5 T [159]. As the magnetic field increased to 7 T, the r_1 slightly decreased and r_2 increased linearly with the field. Zhao et al. synthesized $GdPO_4$ nanorods (up to $\sim$100 nm in length and $\sim$10 nm in diameter) in the presence of PVP molecules [160]. The r_1 of $GdPO_4$ was 2.08 s^{-1} mM^{-1} at 4.7 T. Size-dependent MRI relaxivity of Eu-doped $GdPO_4$ rod-like nanoparticles was investigated by Talham et al. [161]. They found although ionic molar relaxivity decreases for larger particles, the relaxivity per nanoparticle can be significantly greater. By doping light-emitting lanthanide ions into $GdPO_4$ host matrix, bimodal nanoprobe (luminescent and magnetic) could be obtained.

Tan et al. demonstrated a simple synthetic strategy for the fabrication of Tb and Yb/Er doped Gd_2O_3 nanorods [162]. As refluxing progressed, monodispersed quasi-spherical Gd_2O_3 nanocrystals were produced at first, and then fused into nanorods (18.8 ± 5.7 nm in length). The Yb/Er co-doped Gd_2O_3 nanorods exhibit good T_1-weighted MRI contrast enhancing and upconversion fluorescence properties. They also prepared $NaDyF_4$:Yb^{3+}/$NaGdF_4$:Yb^{3+},Er^{3+} nanorods, with the average diameter and length of 21 and 45 nm, respectively [163]. The r_1 (0.321 s^{-1} mM^{-1}) is quite small, and the presence of Dy^{3+} is inferred to affect the T_1 induced by Gd^{3+}. However the r_2 (437.97 s^{-1} mM^{-1}) is much higher than other reported Dy-based materials, probably due to the additional synergistic contribution of T_2 shortening by the Gd^{3+} sitting adjacent to Dy^{3+} in the nanorods.

Jin et al. reported a facile solvothermal approach to synthesize monodispersed ultrathin GdF_3 nanowires (lengths of 20–40 nm and diameters of *ca.* 2 nm) [164]. The nanowires were formed through assembly of GdF_3 nanocrystals. The surface capping ligands anchored to some specific GdF_3 surfaces selectively, and thus facilitated the oriented attachment along the no (or less) capped crystal planes. After modificated with the surfactant Pluronic F127, the GdF_3 nanowires showed high r_1

of 15.0 s^{-1} mM^{-1} at 7 T. The large length in 1D direction and low symmetry of nonspherical structure prolonged their τ_R compared to 0D nanoparticles, which was believed to be responsible for the high r_1.

2D nanostructures have also been well studied. Murray et al. reported shape-controlled synthesis of Gd_2O_3 tripodal and triangular nanoplates [165]. With an increase of magnetic field strength from 9.4 to 14.1 T, the r_1 of PEI-capped Gd_2O_3 tripodal nanoplates decreased from 1.41 to 0.89 s^{-1} mM^{-1}, and r_2 increased from 140 to 193 s^{-1} mM^{-1}. Reduced spectral density at higher magnetic field strengths results in less efficient dipole-dipole relaxation and a corresponding decrease in r_1. The magnetic moment of paramagnetic nanoparticles is proportional to local magnetic field strength, resulting in more effective dephasing of proton and thus increased r_2 at higher fields.

Colvin et al. synthesized Gd_2O_3 nanoplates via a thermal decomposition method [166]. The nanoplates have a core diameter varying from 2 to 22 nm and a thickness of 1–2 nm. When coated with an octylamine modified poly(acrylic acid) polymer layer, the r_1 of 2 nm Gd_2O_3 nanoplates reached 47.2 s^{-1} mM^{-1} at 1.41 T, about 10 times higher than that of Gd-DTPA.

Li et al. reported the synthesis of lanthanide ion doped $GdVO_4$ tetragonal nanosheets (with a thickness of $\sim$5 nm and a width of $\sim$150 nm) using a facile solvothermal reaction [167, 168]. After the ligand exchange reaction with poly (acrylic acid), the hydrophilic nanosheets showed excellent paramagnetic properties (r_1 reached 37.8 s^{-1} mM^{-1} at 0.5 T). This high r_1 was attributed to the special 2D nanostructure, since most of the Gd^{3+} were exposed on the surface of nanosheets and water-soluble polymer coating may offer a hydrophilic interface between the surface of the nanosheets and water molecules.

Alexandrou et al. synthesized Eu-doped $GdVO_4$ nanoparticles which combine magnetic resonance contrast enhancing properties with luminescence properties and hydrogen peroxide sensing features [169]. The 2D projection of the nanoparticles is an ellipse with the two major axes having lengths of 13.1 ± 1.1 and 26.6 ± 4.8 nm, respectively. The paramagnetic nanoparticles showed high r_1 (8.18 s^{-1} mM^{-1}) and r_2 (9.38 s^{-1} mM^{-1}).

5.3.2.2 Ln^{3+}(Other Than Gd^{3+})-Based Anisotropic Nanostructures as MRI CAs

Currently, the development of MRI is towards high field to further increase the signal-to-noise ratio, and to further improve the temporal and spatial resolution [170]. Unfortunately, the efficiencies of current clinically used CAs are reduced when field strength increased to higher than 3 T [145, 171, 172]. Therefore, CAs with high performance under high magnetic field are in urgent need. Paramagnetic trivalent RE^{3+} ions other than Gd^{3+} are less efficient T_1 relaxation agents, mainly

due to their short electronic relaxation time. However, those paramagnetic RE^{3+} with large magnetic moments (such as Tb^{3+}, Dy^{3+}, Ho^{3+} and Er^{3+}) can induce field inhomogeneities, resulting in transverse relaxation enhancement of protons [173]. The r_2 of lanthanide nanoparticles appeared to be proportional to the magnetic field strength and to the square of the effective moment of the lanthanide [174]. Thus, lanthanide-based nanomaterials hold great potential as T_2 CAs for high field MRI [171, 175].

Same with T_1 CAs, relaxivity properties of T_2 CAs are also believed to be influenced significantly by size and shape. van Veggel et al. synthesized $NaDyF_4$ nanoparticles with different sizes, and studied size dependence of r_2 [176]. They found larger nanoparticles show higher r_2 than smaller ones, and attributed this to spin-canting effects. With the decrease in the nanoparticle size, the *S/V* ratio increases and curvature of nanoparticles becomes more pronounced. Spins located near the surface tend to be slightly tilted, resulting in low magnetization value for small nanoparticles. Zeng et al. reported the synthesis of $NaErF_4$ with different shapes and discussed the shape induced magnetic properties [177]. They speculated that the different shape anisotropy leads to the difference of magnetization, and consequently the rod-like morphology had highest magnetization. After doping with Yb^{3+}, multi-functional $NaErF_4$ nanorods were obtained, combining upconversion emission, X-ray attenuation and negative relaxation enhancement properties [178].

Shen et al. reported Co^{2+}-doped $NaYF_4$:Yb^{3+},Tm^{3+} nanorods (mean width of 19.8 nm and mean length of 33.2 nm) as dual-modality imaging nanoprobes [179]. The r_2 of nanorods was up to 1544 s^{-1} mM^{-1}, due to the doping of Co^{2+}. Except the aforementioned sodium lanthanide fluoride, hydroxides with rod-like morphology have also been reported. Lee et al. reported water-soluble and biocompatible D-glucuronic acid coated $Dy(OH)_3$ nanorods (20 × 300 nm) and $Eu(OH)_3$ nanorods (9.0 × 118.3 nm) [180, 181]. The r_1 and r_2 of $Dy(OH)_3$ was 0.97 and 181.57 s^{-1} mM^{-1} at 1.5 T, respectively, while both of r_1 and r_2 were very small for $Eu(OH)_3$, probably due to the insufficient surface coating. To compensate for the deficiencies of individual imaging modalities, $NaDyF_4$ nanorods coated with α-cyclodextrin and modified with Gd-DTPA were prepared by Liao et al. [182] Dy^{3+} in the host matrix induces a high X-ray attenuation ability for CT and negative enhancement for T_2-weighted MRI (r_2 = 7.68 s^{-1} mM^{-1}), while Gd-DTPA induces positive enhancement for T_1-weighted MRI (r_1 = 4.65 s^{-1} mM^{-1}).

Reports of 2D lanthanide-based nanomaterials as MRI CAs are quite rare, probably due to the relatively large *S/V* ratio, which is unfavorable for T_2 CAs as we discussed above. Lanthanide (Gd, Dy and Yb) oxides nanodisks were produced with high-temperature colloidal syntheses by Helms et al. [183]. These nanodisks were 10–14 nm in diameter with a thickness of a single unit cell. For Dy_2O_3 nanodisks, their r_2 values showed *ca.* 1.7-fold enhancement over Gd-DTPA when passivated with poly(acrylic acid)-methoxy-terminated polyethylene oxides alongside Gd-DTPA at 1.41 T.

5.3.3 Catalytic Application of Rare Earth Anisotropic Nanostructures

The catalytic applications of rare earth nanomaterials draw large attention due to the unique electronic structures as rare earth elements possess 4f orbitals without full electron occupancy and lanthanide contraction. In particular, La and Ce are extensively used as catalyst or catalytic components. Among the compounds of La and Ce, ceria is the most representative catalyst and has been widely used in a number of catalytic reactions. Ceria can uptake and release oxygen owing to the transformation between Ce^{3+} and Ce^{4+} [184]. When the size decreases to nanometer scale, ceria exhibits more excellent performances due to high ratio of atoms exposed and thus high specific area. A large number of researches related to the controllable synthesis and applications of ceria nanomaterials have been conducted in the past decade. Therefore, here in this section, we will mainly focus on nanoceria to demonstrate the properties and applications of rare earth nanomaterials.

5.3.3.1 Basic Properties of Ceria Nanocrystals

As mentioned before, CeO_2 crystals are in fluorite structure, consisting of a face-centered cubic (fcc) unit cell of cations with anions occupying the octahedral interstitial sites [185]. In this structure, each cerium cation is coordinated by eight nearest-neighboring oxygen anions, and each oxygen anion is coordinated by four nearest-neighboring cerium cations. Of note, there exist both +3 and +4 oxidation states for cerium, and the transformation between Ce^{3+} and Ce^{4+} is reversible. Ceria can form a non-stoichiometric oxide (CeO_{2-x}) through releasing or uptaking oxygen at the ambient partial pressure of oxygen, while maintaining the crystal structure [186]. However, owing to the transformation between Ce^{3+} and Ce^{4+}, the discrepancy in the number of atomic neighbors and interatomic distances can cause surface defects in ceria, which is often responsible for the catalytic activity of ceria [17]. The main defect in CeO_2 is the formation of oxygen vacancies. The fluorite structure allows oxygen atoms for rapid diffusion as a function of the number of oxygen vacancies. This character endows ceria nanomaterials the capacity to store and release oxygen. In order to maintain the charge balance, the oxygen vacancies form and disappear during the transformation between Ce^{3+} and Ce^{4+} [187]. Oxygen vacancies can be produced via the following defect reaction:

$$\mathrm{Oo} + 2\mathrm{Ce_{Ce}} = 1/2\mathrm{O_2} + \mathrm{V\ddot{o}} + 2\mathrm{Ce'_{Ce}} \quad (1)$$

in which Ce_{Ce}, Oo, Vö and Ce'_{Ce} represent Ce^{4+}, O^{2-}, oxygen vacancies and Ce^{3+}, respectively. Oxygen vacancies play an important role in the activity of ceria nanomaterials for the various catalytic reactions like CO oxidation [188]. Besides the defect properties, ceria also possesses versatile acid–base properties [189].

The defect and acid–base properties are the bases of catalytic applications of ceria nanomaterials.

There are three low-index lattice planes on the surface of CeO_2 nanocrystals: (100), (110) and (111) [185]. According to density functional theory calculations, their stability follows this sequence: (111) > (110) > (100), while their activity follows the opposite order [190, 191]. And the oxygen vacancies are different on three planes. The energy required to generate oxygen vacancies on (111) plane surface is greater than those on (110) and (100) plane surfaces. Therefore, (110) and (100) planes in ceria are favorable in catalytic reactions owing to more vacancies. Generally, the shape of CeO_2 will determine the exposed lattice planes. For example, ceria nanoparticles consisting of octahedra or truncated octahedral shapes mainly expose the most stable (111) facets, while nanorods can be enclosed by (110) and (100) planes, and nanocubes can expose (100) planes. So there are more oxygen vacancies on the surface of nanorods and nanocubes. In view of the intrinsic activity of different planes, the catalytic performance and applications are considered to be closely linked to morphologies of ceria nanomaterials. Recently, ceria nanomaterials have been applied in a number of catalytic reactions, such as carbon monoxide (CO) oxidation, photocatalysis, organic chemistry and bio-anti-oxidation.

5.3.3.2 Catalysis for CO Oxidation

Ceria nanomaterials have been extensively applied in heterogeneous catalysis based on its ability to release and uptake oxygen [192]. CO oxidation is a simple but most extensively studied reaction in heterogeneous catalytic reaction. The reports on catalytic application of ceria nanomaterials for CO oxidation are abundant. Recently, the morphology-dependent catalytic properties of ceria nanomaterials have been investigated including 0D nanostructures (nanocube [193, 194], nanopolyhedron [194]), 1D nanostructures (nanowire [193, 195], nanorod [193, 196], nanotube [193, 196]) and 2D nanostructures (nanoplate [196]).

The morphology-dependent activities toward CO oxidation of ceria nanomaterials are essential for developing advanced catalysts. The activities of ceria toward CO oxidation are regulated through controlling morphologies by the modulation of specific area, exposed facets and oxygen vacancies. Ceria nanomaterials with high specific area which have more active sites show superior catalytic performance [197]. For example, Li et al. [197] prepared CeO_2 hollow spheres via a layer-by-layer method and observed the activity of the CeO_2 hollow spheres was higher than that of the non-hollow counterpart. Furthermore, CeO_2 nanotube also exhibited better catalytic performance in CO oxidation due to the exposed inner and outer surface [198]. Therefore, multifold ceria nanomaterials with high specific area were investigated so as to design favorable catalyst, such as spindle-like CeO_2 [198], platelet-like CeO_2 [199] and mesoporous CeO_2 [200].

However, specific area is not the sole factor influencing the catalytic activity toward CO oxidation. For example, Zhou et al. [22] reported that single CeO_2

nanorods are more active for CO oxidation than irregular nanoparticles. The higher activity was attributed to more exposed reactive crystal planes (100) and (110). Recently, morphology-controlled synthesis of ceria nanomaterials, such as nanocubes, 1D nanomaterials (wire, rods and tubes) and 2D nanomaterials (plates), provide an opportunity for designing excellent catalytic materials with desirable exposed planes. For example, Yan et al. [24] focused on the shape-dependent oxygen storage capacity of ceria nanocrystals with various shapes (nanopolyhedra, exposing (111) and (100); nanorods, (110) and (100), and nanocubes, (100)). The results showed that nanorods and nanocubes were more active than nanopolyhedra. Therefore, the design of highly active catalyst with well-defined crystal planes has been attractive and challenging in CO oxidation. Wu et al. [201, 202] investigated CO oxidation over ceria nanocrystals with defined surface planes including rods, cubes, and octahedra. They revealed that the reducibility of these ceria nanoparticles is in accordance with their CO oxidation activity, following the sequence: rods > cubes > octahedral. In addition, the intrinsic factor for this order was surface oxygen vacancies on different planes. The redox activity of ceria is proposed to be controlled by the nature of the oxygen vacancies which is critical for ceria catalysis. Wu et al. [201] probed defect sites on CeO_2 nanocrystals with well-defined surface planes by Raman spectroscopy and O_2 adsorption. They observed nanorods have the most abundant intrinsic defect sites, followed by nanocubes and nanooctahedra when ceria was oxidized. In addition, when ceria was reduced, more defect sites induced are clustered on nanorods than on nanocubes. However, very few defect sites can be generated on the nanooctahedra due to its lowest reducibility. Moreover, increasing the proportion of active planes is an efficient approach for enhancing the catalytic activity. Both CeO_2 nanorods and CeO_2 nanowires prepared by Tana et al. [203] predominantly exposed the reactive {110} and {100} planes. However, the CeO_2 nanowires exhibited higher activity for CO oxidation than nanorods because CeO_2 nanowires expose a larger proportion of active planes on the surface. Other 1D and 2D ceria nanomaterials were also assessed in CO oxidation, such as CeO_2 nanotubes, spindle-like CeO_2, platelet-like CeO_2, CeO_2 nanoplates. The CO oxidation properties of nanorods, nanoplates, and nanotubes were investigated by Pan et al. [14]. They observed an enhanced catalytic activity for CeO_2 nanoplates compared with CeO_2 nanotubes and nanorods, and the crystal surfaces (100) of CeO_2 nanoplates were considered to play an important role in determining their catalytic oxidation properties.

In addition, even if the morphology of ceria is the same, the activity can be modulated by synthetic conditions. For example, Liu et al. [188] prepared two nanorod samples by changing the precursor. Sample A with exposed (100) and (111) facets showed lower activity than Sample B with exposed (100) and (110) facets. The difference could be attributed to the difference of oxygen defects. Therefore, in summary, the activity of nanoceria for CO oxidation is dependent on the morphology, due to the differences in specific area, exposed planes and oxygen vacancies.

5.3.3.3 Photocatalysis

The researches regarding to photocatalytic applications of ceria nanomaterials are mainly focused on the degradation of organic pollutants, including methylene blue, methyl orange, Congo red and so on [204–207]. For example, Lu et al. [206] reported the application of ceria nanowire in removing the Congo red. In addition, ceria nanomaterials also exhibit activity in photolysis of water [208]. Lu et al. [208] observed that CeO_2 nanorods with (110) planes showed considerable photocatalytic activity for hydrogen evolution due to their redox capacity.

5.3.3.4 Catalysis of Organic Chemistry Reactions

The redox and acid–base properties of ceria are important factors that allow for activating complex organic molecules and selectively orienting their transformation [189]. Sato's group conducted significant research on catalytic application of ceria nanomaterials in organic synthesis, including alcohol dehydration reaction, alkylation reaction, condensation reaction and so on. For example, they reported CeO_2 (111) facets have active sites for the reactions of butanediols and of propanoic acid [209]. In addition, ceria nanomaterials also exhibit excellent catalytic properties in redox organic reaction. Lv et al. [210] reported that CeO_2 nanocube with exposed (100) facets showed exclusive selectivity for the oxidation of toluene to benzaldehydes in liquid phase by O_2. CeO_2 nanoplates prepared by Zhang et al. can selectively catalyze the reduction of nitro-aromatic compounds [211, 212].

5.3.3.5 Catalysis for Anti-oxidation

Recently, ceria nanomaterials attract large attention as an excellent anti-oxidant due to the reversible conversion between Ce^{3+} and Ce^{4+} [213]. It was reported that ceria nanomaterials can promote the decomposition of superoxide anion ($O_2^{\bullet -}$), hydrogen peroxide (H_2O_2) and hydroxyl radical [213–215]. Biologically, owing to the oxygen defects on the surface acting as sites for free radical scavenging, ceria nanoparticles exhibit excellent anti-oxidation performance in protecting cells from radiation, inflammation, ischemic strokes and so on [26, 216–218]. Kim et al. reported that ceria nanoparticles can protect against ischemic stroke [216]. Chen et al. showed that nanoceria particles can prevent increases in the intracellular concentrations of ROIs in primary cell cultures of rat retina and, in vivo, prevent loss of vision due to light-induced degeneration of photoreceptor cells [217]. The results reported by Nel et al. showed that CeO_2 nanoparticles can suppress the generation of reactive oxygen species (ROS) production, induce cellular resistance to an exogenous source of oxidative stress and protect cells from oxidant injury [218].

Most published studies show that nanoceria is well tolerated in living organisms. However, the bio-response was closely linked to the morphology of ceria.

Therefore, the bio-safety of ceria nanomaterials with particular morphology should be concerned, such as nanorods. Nel group conducted the systematic study about the effect of aspect ratio (R) of ceria nanorods on lysosomal damage, cytotoxicity, and 1L-1β production by the human myeloid cell line (THP-1) [26]. Their results showed that short CeO_2 nanorods with R = 1–16 were nontoxic. The nanorods with intermediary aspect ratios (R = 22, 31) did not cause any obvious cell death but did induce IL-1β production. The two nanowire samples with the highest aspect ratio led to significant IL-1β release as well as cell death. They also performed comparative studies in mouse and gastrointestinal tract (GIT) of zebrafish larvae in order to verify this toxicological paradigm for large-aspect-ratio CeO_2 nanoparticles [219].

5.3.3.6 Other Applications

Ceria as catalyst is also applied in other catalytic reactions, such as steam reforming [220], reduction of nitrogen oxide [221], gas sensitivity [222] and so on. Han et al. studied the application of CeO_2 nanotubes in steam reforming reaction [220], and observed that CeO_2 nanotubes showed higher activity than bulk CeO_2. In addition, rare earth composite nanomaterials are also widely used in industrial catalysis acting as catalyst. Besides acting as the active component in catalytic field, CeO_2 possess extensive applications acting as support. For example, the composite catalyst, consisting of CeO_2 and noble metal, was applied in three way catalyst, CO oxidation, reforming reaction, water–gas shift reaction, NO reduction and so on [223–227].

5.4 Perspective

The research field of rare earth based anisotropic nanomaterials has witnessed a rapid development during the past few decades, due to their rich interests in numerous applications. Though tremendous success has been achieved, a few scientific challenges are yet to be addressed:

(1) Synthesis mechanism. The synthesis mechanism for plenty of systems remain unclear or ambiguous, or simply still in the phase of presumption. This issue is largely owing to the lack of powerful, in situ and real-time characterization tools to monitor and document the reaction process. Therefore, developing some general and highly sensitive on-line monitoring methodologies is urgently necessary for investigating the synthesis mechanism. And undoubtedly, a more in-depth understanding of the synthesis mechanism would help scientists to design synthetic routes for nanostructures with desired morphologies, even those thermodynamically unfavorable ones.

(2) Synthetic methods. The synthetic methods developed so far generally require stringent conditions, such as high temperature, high pressure and inert gas atmosphere. In addition, quite a few methods have to be conducted in non-aqueous solutions, affording nanoparticles with strong hydrophobicity and poor biocompatibility. And up to date, most synthetic procedures are performed only in the lab in small batches, and can hardly be scaled up to an industrially relevant level. Therefore, the research field still calls for advanced synthetic methods that are green, facile, high-throughput, and readily scalable.
(3) Defect management. Defects in/on nanocrystals are inevitable, and can have both positive and negative effects. For optical applications, it is generally expected that the phosphors should possess good crystallinity and minimal defects, and display high luminescence efficiency; whereas for catalysis applications, defects in/on nanocrystals can usually serve as active catalytic sites owing to their inherent high-energy states. Therefore, it is still desired to develop novel methods for effectively annihilating or generating defects in/on nanocrystals, whether during or after the synthesis.

References

1. Q. Su, *Rare Earth Chemistry* (Henan Science and Technology Press, Zhengzhou, 1993)
2. G.X. Xu (ed.), *Rare Earth*, vol. 1. (Metallurgical Industry Press, Beijing, 1995)
3. G.H. Liu (ed.), *Rare Earth Materials Science* (Chemical Industry Press, Beijing, 2007)
4. G. Brunton, The crystal structure of KBF_4. J. Am. Chem. Soc. **25**, 2161–2162 (1969)
5. J.H. Burns, Crystal structure of hexagonal sodium neodymium fluoride and related compounds. Inorg. Chem. **6**, 881–886 (1965)
6. R.E. Thoma, C.F. Weaver, H.A. Friedman, Phase equilibria in the system LiF-YF3. J. Phys. Chem. **65**, 1096–1099 (1961)
7. R.E. Thoma, H. Insley, G.M. Hebert, The sodium fluoride-lanthanide trifluride systems. Inorg. Chem. **7**, 1222–1229 (1966)
8. Q. Su (ed.), *Rare Earth Chemistry* (Henan Science and Technology Press, Zhengzhou, 1993)
9. K.A. Gschneidner (ed.), *Handbook on the Physics and Chemistry of Rare Earths* (Elsevier, Amsterdam, 2011)
10. M.S. Wickleder, Inorganic lanthanide compounds with complex anions. Chem. Rev. **102**, 2011–2087 (2002)
11. C.H. Yan, Z.G. Yan, Y.P. Du, J. Shen, C. Zhang, W. Feng, L.D. Sun, Y.W. Zhang, *Handbook on the Physics and Chemistry of Rare Earths*, vol. 999. Controlled Synthesis and Properties of Rare Earth Based Nanomaterials (Elsevier, 2009)
12. C.H. Yan, C. Zhang, L.D. Sun, *Rare Earth Nanotechnology*. Synthesis of Rare Earth Nanomaterials (Pan Stanford Publishing Pte. Ltd., 2012)
13. Y. Xia, P. Yang, Y. Sun, Y. Wu, B. Mayers, B. Gates, Y. Yin, F. Kim, H. Yan, One-dimensional nanostructures: synthesis, characterization, and applications. Adv. Mater. **15**, 353–389 (2003)
14. Y.W. Jun, J.S. Choi, J. Cheon, Shape control of semiconductor and metal oxide nanocrystals through nonhydrolytic colloidal routes. Angew. Chem. Int. Ed. **45**, 3414–3439 (2006)
15. Z.G. Yan, C.H. Yan, Controlled synthesis of rare earth nanostructures. J. Mater. Chem. **18**, 5046–5059 (2008)

16. Q. Yuan, H.H. Duan, L.L. Li, L.D. Sun, Y.W. Zhang, C.H. Yan, Controlled synthesis and assembly of ceria-based nanomaterials. J. Colloid Interface Sci. **335**, 151–167 (2009)
17. C.W. Sun, H. Li, L.Q. Chen, Nanostructured ceria-based materials: synthesis, properties, and applications. Energy Environ. Sci. **5**, 8475–8505 (2012)
18. R.J. La, Z.A. Hu, H.L. Li, X.L. Shang, Y.Y. Yang, Template synthesis of CeO_2 ordered nanowire arrays. Mater. Sci. Eng. A **368**, 145–148 (2004)
19. G.S. Wu, T. Xie, X.Y. Yuan, B.C. Cheng, L.D. Zhang, An improved sol–gel template synthetic route to large-scale CeO_2 nanowires. Mater. Res. Bull. **39**, 1023–1028 (2004)
20. L. González-Rovira, J.M. Sánchez-Amaya, M. López-Haro, E. del Rio, A.B. Hungría, P. Midgley, J.J. Calvino, S. Bernal, F.J. Botana, Single-step process to prepare CeO_2 nanotubes with improved catalytic activity. Nano Lett. **9**, 1395–1400 (2009)
21. C.W. Sun, H. Li, H.R. Zhang, Z.X. Wang, L.Q. Chen, Controlled synthesis of CeO_2 nanorods by a solvothermal method. Nanotechnology **16**, 1454–1463 (2005)
22. K. Zhou, X. Wang, X. Sun, Q. Peng, Y. Li, Enhanced catalytic activity of ceria nanorods from well-defined reactive crystal planes. J. Catal. **229**, 206–212 (2005)
23. A. Vantomme, Z.Y. Yuan, G.H. Du, B.L. Su, Surfactant-assisted large-scale preparation of crystalline CeO_2 nanorods. Langmuir **21**, 1132–1135 (2005)
24. H.X. Mai, L.D. Sun, Y.W. Zhang, R. Si, W. Feng, H.P. Zhang, H.C. Liu, C.H. Yan, Shape-selective synthesis and oxygen storage behavior of ceria nanopolyhedra, nanorods, and nanocubes. J. Phys. Chem. B **109**, 24380–24385 (2005)
25. J. Ke, J.W. Xiao, W. Zhu, H. Liu, R. Si, Y.W. Zhang, C.H. Yan, Dopant-induced modification of active site structure and surface bonding mode for high-performance nanocatalysts: CO oxidation on capping-free (110)-oriented CeO_2: Ln (Ln = La-Lu) nanowires. J. Am. Chem. Soc. **135**, 15191–15200 (2013)
26. Z. Ji, X. Wang, H. Zhang, S. Lin, H. Meng, B. Sun, S. George, T. Xia, A.E. Nel, J.I. Zink, Designed synthesis of CeO_2 nanorods and nanowires for studying toxicological effects of high aspect ratio nanomaterials. ACS Nano **6**, 5366–5380 (2012)
27. S. Iijima, Helical microtubules of graphitic carbon. Nature **354**, 56–58 (1991)
28. W.Q. Han, L. Wu, Y. Zhu, Formation and oxidation state of CeO_{2-x} nanotubes. J. Am. Chem. Soc. **127**, 12814–12815 (2005)
29. K. Zhou, Z. Yang, S. Yang, Highly reducible CeO_2 nanotubes. Chem. Mater. **19**, 1215–1217 (2007)
30. J.Y. Chane-Ching, F. Cobo, D. Aubert, H.G. Harvey, M. Airiau, A. Corma, A general method for the synthesis of nanostructured large-surface-area materials through the self-assembly of functionalized nanoparticles. Chem. Eur. J. **11**, 979–987 (2005)
31. A.S. Karakoti, S.V.N.T. Kuchibhatla, D.R. Baer, S. Thevuthasan, D.C. Sayle, S. Seal, Self-assembly of cerium oxide nanostructures in ice molds. Small **4**, 1210–1216 (2008)
32. R. Si, Y.W. Zhang, L.P. You, C.H. Yan, Self-organized monolayer of nanosized ceria colloids stabilized by poly(vinylpyrrolidone). J. Phys. Chem. B **110**, 5994–6000 (2006)
33. Q. Yuan, Q. Liu, W.G. Song, W. Feng, W.L. Pu, L.D. Sun, Y.W. Zhang, C.H. Yan, Ordered mesoporous $Ce_{1-x}Zr_xO_2$ solid solutions with crystalline walls. J. Am. Chem. Soc. **129**, 6698–6699 (2007)
34. H. Wang, Q.L. Huang, J.M. Hong, X.T. Chen, Z.L. Xue, Selective synthesis and characterization of nanocrystalline EuF_3 with orthorhombic and hexagonal structures. Cryst. Growth Des. **6**, 1972–1974 (2006)
35. H. Wang, Q.L. Huang, J.M. Hong, X.T. Chen, Z.L. Xue, Controlled synthesis and characterization of nanostructured EuF_3 with different crystalline phases and morphologies. Cryst. Growth Des. **6**, 2169–2173 (2006)
36. X. Wang, J. Zhuang, Q. Peng, Y.D. Li, Hydrothermal synthesis of rare-earth fluoride nanocrystals. Inorg. Chem. **45**, 6661–6665 (2006)
37. X. Liang, X. Wang, J. Zhuang, Q. Peng, Y.D. Li, Synthesis of $NaYF_4$ nanocrystals with predictable phase and shape. Adv. Funct. Mater. **17**, 2757–2765 (2007)
38. X. Liang, X. Wang, J. Zhuang, Q. Peng, Y.D. Li, Branched $NaYF_4$ nanocrystals with luminescent properties. Inorg. Chem. **46**, 6050–6055 (2007)

39. L.Y. Wang, P. Li, Y.D. Li, Down- and up-conversion luminescent nanorods. Adv. Mater. **19**, 3304–3307 (2007)
40. J.H. Zeng, J. Su, Z.H. Li, R.X. Yan, Y.D. Li, Synthesis and upconversion luminescence of hexagonal-phase $NaYF_4$:Yb, Er^{3+} phosphors of controlled size and morphology. Adv. Mater. **17**, 2119–2123 (2005)
41. M.F. Zhang, H. Fan, B.J. Xi, X.Y. Wang, C. Dong, Y.T. Qian, Synthesis, characterization, and luminescence properties of uniform Ln^{3+}-doped YF_3 nanospindles. J. Phys. Chem. C **111**, 6652–6657 (2007)
42. F. Zhang, Y. Wan, T. Yu, F.Q. Zhang, Y.F. Shi, S.H. Xie, Y.G. Li, L. Xu, B. Tu, D.Y. Zhao, Uniform nanostructured arrays of sodium rare-earth fluorides for highly efficient multicolor upconversion luminescence. Angew. Chem. Int. Ed. **46**, 7976–7979 (2007)
43. H.X. Mai, Y.W. Zhang, R. Si, Z.G. Yan, L.D. Sun, L.P. You, C.H. Yan, High-quality sodium rare-earth fluoride nanocrystals: controlled synthesis and optical properties. J. Am. Chem. Soc. **128**, 6426–6436 (2006)
44. Y.P. Du, Y.W. Zhang, Z.G. Yan, L.D. Sun, C.H. Yan, Highly luminescent self-organized sub-2-nm EuOF nanowires. J. Am. Chem. Soc. **131**, 16364–16365 (2009)
45. Z.G. Yan, Y.W. Zhang, L.P. You, R. Si, C.H. Yan, General synthesis and characterization of monocrystalline 1D-nanomaterials of hexagonal and orthorhombic lanthanide orthophosphate hydrate. J. Cryst. Growth **262**, 408–414 (2004)
46. Y.W. Zhang, Z.G. Yan, L.P. You, R. Si, C.H. Yan, General synthesis and characterization of monocrystalline lanthanide orthophosphate nanowires. Eur. J. Inorg. Chem. **2003**, 4099–4104 (2003)
47. H. Meyssamy, K. Riwotzki, A. Kornowski, S. Naused, M. Haase, Wet-chemical synthesis of doped colloidal nanomaterials: particles and fibers of $LaPO_4$:Eu, $LaPO_4$:Ce, and $LaPO_4$:Ce, Tb. Adv. Mater. **11**, 840–844 (1999)
48. M. Yang, H. You, K. Liu, Y. Zheng, N. Guo, H. Zhang, Low-temperature coprecipitation synthesis and luminescent properties of $LaPO_4$:Ln^{3+}(Ln^{3+}=Ce^{3+}, Tb^{3+}) nanowires and $LaPO_4$:Ce^{3+}, Tb^{3+}/$LaPO_4$ core/shell nanowires. Inorg. Chem. **49**, 4996–5002 (2010)
49. W.H. Di, X.X. Zhao, S.Z. Lu, X.J. Wang, H.F. Zhao, Thermal and photoluminescence properties of hydrated YPO_4:Eu^{3+} nanowires. J. Solid State Chem. **180**, 2478–2484 (2007)
50. R.X. Yan, Y.D. Li, Down/up conversion in Ln^{3+}-Doped YF_3 nanocrystals. Adv. Funct. Mater. **15**, 763–770 (2005)
51. Y.P. Fang, A.W. Xu, R.Q. Song, H.X. Zhang, L.P. You, J.C. Yu, H.Q. Liu, Systematic synthesis and characterization of single-crystal lanthanide orthophosphate nanowires. J. Am. Chem. Soc. **125**, 16025–16034 (2003)
52. Y.P. Fang, A.W. Xu, A.M. Qin, R.J. Yu, Selective synthesis of hexagonal and tetragonal dysprosium orthophosphate nanorods by a hydrothermal method. Cryst. Growth Des. **5**, 1221–1225 (2005)
53. W.B. Bu, H.R. Chen, Z.L. Hua, Z.C. Liu, W.M. Huang, L.X. Zhang, J.L. Shi, Surfactant-assisted synthesis of Tb(III)-doped cerium phosphate single-crystalline nanorods with enhanced green emission. Appl. Phys. Lett. **85**, 4307–4309 (2004)
54. W.B. Bu, L.X. Zhang, Z.L. Hua, H.R. Chen, J.L. Shi, Synthesis and characterization of uniform spindle-shaped microarchitectures self-assembled from aligned single-crystalline nanowires of lanthanum phosphates. Cryst. Growth Des. **7**, 2305–2309 (2007)
55. Y. Xing, M. Li, S.A. Davis, S. Mann, Synthesis and characterization of cerium phosphate nanowires in microemulsion reaction media. J. Phys. Chem. B **110**, 1111–1113 (2006)
56. P. Ghosh, J. Oliva, E. De la Rosa, K.K. Haldar, D. Solis, A. Patra, Enhancement of upconversion emission of $LaPO_4$:Er@Yb core−shell nanoparticles/nanorods. J. Phys. Chem. C **112**, 9650–9658 (2008)
57. Z.Y. Huo, C. Chen, D. Chu, H.H. Li, Y.D. Li, Systematic synthesis of lanthanide phosphate nanocrystals. Chem. Eur. J. **13**, 7708–7714 (2007)
58. H.X. Mai, Y.W. Zhang, L.D. Sun, C.H. Yan, Orderly aligned and highly luminescent monodisperse rare-earth orthophosphate nanocrystals synthesized by a limited anion-exchange reaction. Chem. Mater. **19**, 4514–4522 (2007)

59. G.C. Li, K. Chao, H.R. Peng, K.Z. Chen, Z.K. Zhang, Facile synthesis of $CePO_4$ nanowires attached to CeO_2 octahedral micrometer crystals and their enhanced photoluminescence properties. J. Phys. Chem. C **112**, 16452–16456 (2008)
60. W.L. Fan, W. Zhao, L.P. You, X.Y. Song, W.M. Zhang, H.Y. Yu, S.X. Sun, A simple method to synthesize single-crystalline lanthanide orthovanadate nanorods. J. Solid State Chem. **177**, 4399–4403 (2004)
61. C.J. Jia, L.D. Sun, Z.G. Yan, Y.C. Pang, S.Z. Lü, C.H. Yan, Monazite and zircon type $LaVO_4$:Eu nanocrystals-synthesis, luminescent properties, and spectroscopic identification of the Eu^{3+} sites. Eur. J. Inorg. Chem. **18**, 2626–2635 (2010)
62. C.J. Jia, L.D. Sun, F. Luo, X.C. Jiang, L.H. Wei, C.H. Yan, Structural transformation induced improved luminescent properties for $LaVO_4$: Eu Nanocrystals. Appl. Phys. Lett. **84**, 5305–5307 (2004)
63. C.J. Jia, L.D. Sun, L.P. You, X.C. Jiang, F. Luo, Y.C. Pang, C.H. Yan, Selective synthesis of monazite- and zircon-type $LaVO_4$ nanocrystals. J. Phys. Chem. B **109**, 3284–3290 (2005)
64. W.L. Fan, X.Y. Song, S.X. Sun, X. Zhao, Microemulsion-mediated hydrothermal synthesis and characterization of zircon-type $LaVO_4$ nanowires. J. Solid State Chem. **180**, 284–290 (2007)
65. K.S. Novoselov, A.K. Geim, S.V. Morozov, D. Jiang, Y. Zhang, S.V. Dubonos, I.V. Grigorieva, A.A. Firsov, Electric field effect in atomically thin carbon films. Science **306**, 666–669 (2004)
66. H. Li, J. Wu, Z. Yin, H. Zhang, Preparation and applications of mechanically exfoliated single-layer and multilayer MoS_2 and WSe_2 nanosheets. Acc. Chem. Res. **47**, 1067–1075 (2014)
67. M. Chhowalla, H.S. Shin, G. Eda, L.-J. Li, K.P. Loh, H. Zhang, The chemistry of two-dimensional layered transition metal dichalcogenide nanosheets. Nat. Chem. **5**, 263–275 (2013)
68. Q.H. Wang, K. Kalantar-Zadeh, A. Kis, J.N. Coleman, M.S. Strano, Electronics and optoelectronics of two-dimensional transition metal dichalcogenides. Nat. Nano. **7**, 699–712 (2012)
69. H. Imagawa, S.H. Sun, Controlled synthesis of monodisperse CeO_2 nanoplates developed from assembled nanoparticles. J. Phys. Chem. C **116**, 2761–2765 (2012)
70. X.H. Guo, C.C. Mao, J. Zhang, J. Huang, W.N. Wang, Y.H. Deng, Y.Y. Wang, Y. Cao, W. X. Huang, S.H. Yu, Cobalt-doping-induced synthesis of ceria nanodisks and their significantly enhanced catalytic activity. Small **8**, 1515–1520 (2012)
71. R. Si, Y.W. Zhang, L.P. You, C.H. Yan, Rare-earth oxide nanopolyhedra, nanoplates, and nanodisks. Angew. Chem. Int. Ed. **44**, 3256–3260 (2005)
72. R. Si, Y.W. Zhang, H.P. Zhou, L.D. Sun, C.H. Yan, Controlled-synthesis, self-assembly behavior, and surface-dependent optical properties of high-quality rare-earth oxide nanocrystals. Chem. Mater. **19**, 18–27 (2006)
73. D. Wang, Y. Kang, V. Doan-Nguyen, J. Chen, R. Küngas, N.L. Wieder, K. Bakhmutsky, R.J. Gorte, C.B. Murray, Synthesis and oxygen storage capacity of two-dimensional ceria nanocrystals. Angew. Chem. Int. Ed. **50**, 4378–4381 (2011)
74. T. Yu, B. Lim, Y. Xia, Aqueous-phase synthesis of single-crystal ceria nanosheets. Angew. Chem. Int. Ed. **49**, 4484–4487 (2010)
75. Y. Sun, Q. Liu, S. Gao, H. Cheng, F. Lei, Z. Sun, Y. Jiang, H. Su, S. Wei, Y. Xie, Pits confined in ultrathin cerium(IV) oxide for studying catalytic centers in carbon monoxide oxidation. Nat. Commun. **4**, 2899–2907 (2013)
76. H. Hu, Z.G. Chen, T.Y. Cao, Q. Zhang, M.G. Yu, F.Y. Li, T. Yi, C.H. Huang, Hydrothermal synthesis of hexagonal lanthanide-doped LaF_3 nanoplates with bright upconversion luminescence. Nanotechnology **19**, 375702 (2008)
77. Y.W. Zhang, X. Sun, R. Si, L.P. You, C.H. Yan, Single-crystalline and monodisperse LaF_3 triangular nanoplates from a single-source precursor. J. Am. Chem. Soc. **127**, 3260–3261 (2005)

78. Y.P. Du, Y.W. Zhang, L.D. Sun, C.H. Yan, Atomically efficient synthesis of self-assembled monodisperse and ultrathin lanthanide oxychloride nanoplates. J. Am. Chem. Soc. **131**, 3162–3163 (2009)
79. H.P. Zhou, C. Zhang, C.H. Yan, Controllable assembly of diverse rare-earth nanocrystals via the Langmuir-Blodgett technique and the underlying size- and symmetry-dependent assembly kinetics. Langmuir **25**, 12914–12925 (2009)
80. L.W. Qian, J. Zhu, Z. Chen, Y.C. Gui, Q. Gong, Y.P. Yuan, J.T. Zai, X.F. Qian, Self-assembled heavy lanthanide orthovanadate architecture with controlled dimensionality and morphology. Chem. Eur. J. **15**, 1233–1240 (2009)
81. J.F. Liu, Y.D. Li, Synthesis and self-assembly of luminescent Ln^{3+}-doped $LaVO_4$ uniform nanocrystals. Adv. Mater. **19**, 1118–1122 (2007)
82. J.F. Liu, Y.D. Li, General synthesis of colloidal rare earth orthovanadate nanocrystals. J. Mater. Chem. **17**, 1797–1803 (2007)
83. J.-C.G. Bünzli, C. Piguet, Taking advantage of luminescent lanthanide ions. Chem. Soc. Rev. **34**, 1048–1077 (2009)
84. J. Shen, L.D. Sun, C.H. Yan, Luminescent rare earth nanomaterials for bioprobe applications. Dolton Trans. **42**, 5687–5697 (2008)
85. S. Ye, F. Xiao, Y.X. Pan, Y.Y. Ma, Q.Y. Zhang, Phosphors in phosphor-converted white light-emitting diodes: recent advances in materials, techniques and properties. Mater. Sci. Eng. A **71**, 1–34 (2010)
86. J.W. Stouwdam, F.C.J.M. van Veggel, Near-infrared emission of redispersible Er^{3+}, Nd^{3+}, and Ho^{3+} doped LaF_3 nanoparticles. Nano Lett. **7**, 733–737 (2002)
87. J. Shen, L.D. Sun, J.D. Zhu, L.H. Wei, H.F. Sun, C.H. Yan, Biocompatible bright YVO_4: Eu nanoparticles as versatile optical bioprobes. Adv. Funct. Mater. **20**, 3708–3714 (2010)
88. C.-J. Carling, F. Nourmohammadian, J.-C. Boyer, N.R. Branda, Remote-control photorelease of caged compounds using near-infrared light and upconverting nanoparticles. Angew. Chem. Int. Ed. **49**, 3782–3785 (2010)
89. L.T. Su, S.K. Karuturi, J.S. Luo, L.J. Liu, X.F. Liu, J. Guo, T.C. Sum, R.R. Deng, H.J. Fan, X.G. Liu, A.L.Y. Tok, Photon upconversion in hetero-nanostructured photoanodes for enhanced near-Infrared light harvesting. Adv. Mater. **25**, 1603–1607 (2013)
90. W.-Y. Huang, F. Yoshimura, K. Ueda, Y. Shimomura, H.-S. Sheu, T.-S. Chan, H.F. Greer, W.Z. Zhou, S.-F. Hu, R.-S. Liu, J.P. Attfield, Nanosegregation and neighbor-cation control of photoluminescence in carbidonitridosilicate phosphors. Angew. Chem. Int. Ed. **52**, 8012–8016 (2013)
91. Z.H. Xu, X.J. Kang, C.X. Li, Z.Y. Hou, C.M. Zhang, D.M. Yang, G.G. Li, J. Lin, Ln^{3+} (Ln = Eu, Dy, Sm, and Er) ion-doped YVO4 nano/microcrystals with multiform morphologies: hydrothermal synthesis, growing mechanism, and luminescent properties. Inorg. Chem. **49**, 6706–6715 (2010)
92. X.G. Zhang, L.Y. Zhou, Q. Pang, J.X. Shi, M.L. Gong, Tunable luminescence and $Ce^{3+} \rightarrow Tb^{3+} \rightarrow Eu^{3+}$ energy transfer of broadband-excited and narrow line red emitting Y_2SiO_5:Ce^{3+}, Tb^{3+}, Eu^{3+} Phosphor. J. Phys. Chem. C **118**, 7591–7598 (2014)
93. Y.S. Liu, S.Y. Zhou, D.T. Tu, Z. Chen, M.D. Huang, H.M. Zhu, E. Ma, X.Y. Chen, Amine-functionalized lanthanide-doped zirconia nanoparticles: optical spectroscopy, time-resolved fluorescence resonance energy transfer biodetection, and targeted imaging. J. Am. Chem. Soc. **134**, 15083–15090 (2012)
94. Q.Y. Zhang, X.Y. Huang, Recent progress in quantum cutting phosphors. Prog. Mater Sci. **55**, 353–427 (2010)
95. R.T. Wegh, H. Donker, K.D. Oskam, A. Meijerink, Visible quantum cutting in $LiGdF_4$:Eu^{3+} through downconversion. Science **283**, 663–666 (1999)
96. B.M. van der Ende, L. Aarts, A. Meijerink, Lanthanide ions as spectral converters for solar cells. Phys. Chem. Chem. Phys. **11**, 11081–11095 (2009)
97. F. Auzel, Upconversion and anti-stokes processes with f and d ions in solids. Chem. Rev. **104**, 139–173 (2004)

98. F. Wang, X.G. Liu, Recent advances in the chemistry of lanthanide-doped upconversion nanocrystals. Chem. Soc. Rev. **38**, 976–989 (2009)
99. M. Haase, H. Schäfer, Upconverting nanoparticles. Angew. Chem. Int. Ed. **50**, 5808–5829 (2011)
100. H. Dong, L.D. Sun, C.H. Yan, Basic understanding of the lanthanide related upconversion emissions. Nanoscale **5**, 5703–5714 (2013)
101. N. Menyuk, K. Dwight, J.W. Pierce, NaYF4:Yb, Er-an efficient upconversion phosphor. Appl. Phys. Lett. **21**, 159–161 (1972)
102. S. Heer, K. Krömpe, H.-U. Güdel, M. Haase, Highly efficient multicolor upconversion emission in transparent colloids of lanthanide-doped $NaYF_4$ nanocrystals. Adv. Mater. **16**, 2102–2105 (2004)
103. G.F. Wang, Q. Peng, Y.D. Li, Upconversion luminescence of monodisperse CaF_2:Yb^{3+}/Er^{3+} nanocrystals. J. Am. Chem. Soc. **131**, 14200–14201 (2010)
104. H.X. Mai, Y.W. Zhang, L.D. Sun, C.H. Yan, Highly efficient multicolor up-conversion emissions and their mechanisms of monodisperse NaYF4:Yb, Er core and core/shell-structured nanocrystals. J. Phys. Chem. C **111**, 13721–13729 (2007)
105. J.C. Boyer, F. Vetrone, J.A. Capobianco, A. Speghini, M. Bettinelli, Yb^{3+} ion as a sensitizer for the upconversion luminescence in nanocrystalline $Gd_3Ga_5O_{12}$:Ho^{3+}. Chem. Phys. Lett. **390**, 403–407 (2004)
106. A.X. Yin, Y.W. Zhang, L.D. Sun, C.H. Yan, Colloidal synthesis and blue based multicolor upconversion emissions of size and composition controlled monodisperse hexagonal $NaYF_4$: Yb, Tm nanocrystals. Nanoscale **2**, 953–959 (2010)
107. J.J. Zhou, G.X. Chen, E. Wu, G. Bi, B.T. Wu, Y. Teng, S.F. Zhou, J.R. Qiu, Ultrasensitive polarized up-conversion of Tm_{3+}−Yb_{3+} doped β-$NaYF_4$ single nanorod. Nano Lett. **13**, 2241–2246 (2013)
108. H.X. Mai, Y.W. Zhang, L.D. Sun, C.H. Yan, Size- and phase-controlled synthesis of monodisperse $NaYF_4$:Yb, Er nanocrystals from a unique delayed nucleation pathway monitored with upconversion spectroscopy. J. Phys. Chem. C **111**, 13730–13739 (2007)
109. Y.P. Du, Y.W. Zhang, Z.G. Yan, L.D. Sun, S. Gao, C.H. Yan, Single-crystalline and near-monodispersed $NaMF_3$ (M = Mn Co, Ni, Mg) and $LiMAlF_6$ (M = Ca, Sr) nanocrystals from cothermolysis of multiple trifluoroacetates in solution. Chem. Asian J. **2**, 965–974 (2007)
110. F. Wang, L.D. Sun, J. Gu, Y.F. Wang, W. Feng, Y. Yang, J.F. Wang, C.H. Yan, Selective heteroepitaxial nanocrystal growth of rare earth fluorides on sodium chloride: synthesis and density functional calculations. Angew. Chem. Int. Ed. **51**, 8796–8799 (2012)
111. Y.J. Ding, X. Teng, H. Zhu, L.L. Wang, W.B. Pei, J.J. Zhu, L. Huang, W. Huang, Orthorhombic KSc_2F_7:Yb/Er nanorods: controlled synthesis and strong red upconversion emission. Nanoscale **5**, 11928–11932 (2013)
112. J. Wang, R.R. Deng, M.A. MacDonald, B. Chen, J.K. Yuan, F. Wang, D.Z. Chi, T.S.A. Hor, P. Zhang, G.K. Liu, Y. Han, X.G. Liu, Enhancing multiphoton upconversion through energy clustering at sublattice level. Nat. Mater. **13**, 157–162 (2014)
113. G.F. Wang, Q. Peng, Y.D. Li, Luminescence tuning of upconversion nanocrystals. Chem. Eur. J. **16**, 4923–4931 (2010)
114. L.J. Huang, L.L. Wang, X.J. Xue, D. Zhao, G.S. Qin, W.P. Qin, Enhanced red upconversion luminescence in Er–Tm codoped $NaYF_4$ phosphor. J. Nanosci. Nanotechnol. **11**, 9498–9501 (2011)
115. C. Zhang, J.Y. Lee, Prevalence of anisotropic shell growth in rare earth core-shell upconversion nanocrystals. ACS Nano **7**, 4393–4402 (2013)
116. Y.H. Zhang, L.X. Zhang, R.R. Deng, J. Tian, Y. Zong, D.Y. Jin, X.G. Liu, Multicolor barcoding in a single upconversion crystal. J. Am. Chem. Soc. **136**, 4893–4896 (2014)
117. W. Feng, L.D. Sun, C.H. Yan, Ag nanowires enhanced upconversion emission of $NaYF_4$:Yb, Er nanocrystals via a direct assembly method. Chem. Commun. **29**, 4393–4395 (2009)
118. N.J. Greybush, M. Saboktakin, X.C. Ye, C.D. Giovampaola, S.J. Oh, N.E. Berry, N. Engheta, C.B. Murray, C.R. Kagan, Luminescence in single nanophosphornanorod

heterodimers formed through template-assisted self-assembly. ACS Nano **8**, 9482–9491 (2014)
119. J.Y. Dong, J.I. Zink, Taking the temperature of the interiors of magnetically heated nanoparticles. ACS Nano **8**, 5199–5207 (2014)
120. Y.F. Wang, G.Y. Liu, L.D. Sun, J.W. Xiao, J.C. Zhou, C.H. Yan, Nd^{3+}-sensitized upconversion nanophosphors: efficient *in vivo* bioimaging probes with minimized heating effect. ACS Nano **7**, 7200–7206 (2013)
121. H.L. Wen, H. Zhu, X. Chen, T.F. Hung, B.L. Wag, G.Y. Zhu, S.F. Yu, F. Wang, Upconverting near-infrared light through energy management in core–shell–shell nanoparticles. Angew. Chem. Int. Ed. **52**, 13419–13423 (2013)
122. J. Shen, G.Y. Chen, A.-M. Vu, W. Fan, O.S. Bilsel, C.-C. Chang, G. Han, Engineering the upconversion nanoparticle excitation wavelength: cascade sensitization of tri-doped upconversion colloidal nanoparticles at 800 nm. Adv. Opt. Mater. **1**, 644–650 (2013)
123. X.J. Xie, N.Y. Gao, R.R. Deng, Q. Sun, Q.H. Xu, X.G. Liu, Mechanistic investigation of photon upconversion in Nd^{3+}-sensitized core−shell nanoparticles. J. Am. Chem. Soc. **135**, 12608–12611 (2013)
124. J. Zhou, Z. Liu, F.Y. Li, Upconversion nanophosphors for small-animal imaging. Chem. Soc. Rev. **41**, 1323–1349 (2012)
125. Z.J. Gu, L. Yan, G. Tian, S.J. Li, Z.F. Chai, Y.L. Zhao, Recent advances in design and fabrication of upconversion nanoparticles and their safe theranostic applications. Adv. Mater. **25**, 3758–3779 (2013)
126. H.C. Guo, S.Q. Sun, Lanthanide-doped upconverting phosphors for bioassay and therapy. Nanoscale **4**, 6692–6706 (2012)
127. X.Y. Huang, S.Y. Han, W. Huang, X.G. Liu, Enhancing solar cell efficiency: the search for luminescent materials as spectral converters. Chem. Soc. Rev. **42**, 173–201 (2013)
128. B. Yan, J.-C. Boyer, N.R. Branda, Y. Zhao, Near-infrared light-triggered dissociation of block copolymer micelles using upconverting nanoparticles. J. Am. Chem. Soc. **133**, 19714–19717 (2011)
129. Y.F. Wang, L.D. Sun, J.W. Xiao, W. Feng, J.C. Zhou, J. Shen, C.H. Yan, Rare-earth nanoparticles with enhanced upconversion emission and suppressed rare-earth-ion leakage. Chem. Eur. J. **18**, 5558–5564 (2012)
130. S.F. Lim, R. Riehn, W.S. Ryu, N. Khanarian, C.-K. Tung, D. Tank, R.H. Austin, In vivo and scanning electron microscopy imaging of upconverting nanophosphors in *Caenorhabditis elegans*. Nano Lett. **6**, 169–174 (2006)
131. D.K. Chatterjee, A.J. Rufihah, Y. Zhang, Upconversion fluorescence imaging of cells and small animals using lanthanide doped nanocrystals. Biomaterials **29**, 937–943 (2009)
132. T.S. Yang, Y. Sun, Q. Liu, W. Feng, P.Y. Yang, F.Y. Li, Cubic sub-20 nm $NaLuF_4$-based upconversion nanophosphors for high-contrast bioimaging in different animal species. Biomaterials **33**, 3733–3742 (2012)
133. J.C. Zhou, Z.L. Yang, W. Dong, R.J. Tang, L.D. Sun, C.H. Yan, Bioimaging and toxicity assessments of near-infrared upconversion luminescent $NaYF_4$:Yb, Tm nanocrystals. Biomaterials **32**, 9059–9067 (2011)
134. Q. Liu, Y. Sun, T.S. Yang, W. Feng, C.G. Li, F.Y. Li, Sub-10 nm hexagonal lanthanide-doped $NaLuF_4$ upconversion nanocrystals for sensitive bioimaging in vivo. J. Am. Chem. Soc. **133**, 17122–17125 (2011)
135. L. Cheng, K. Yang, Y.G. Li, J.H. Chen, C. Wang, M.W. Shao, S.-T. Lee, Z. Liu, Facile preparation of multifunctional upconversion nanoprobes for multimodal imaging and dual-targeted photothermal therapy. Angew. Chem. **123**, 7523–7528 (2011)
136. X.F. Qiao, J.C. Zhou, J.W. Xiao, Y.F. Wang, L.D. Sun, C.H. Yan, Triple-functional core–shell structured upconversion luminescent nanoparticles covalently grafted with photosensitizer for luminescent, magnetic resonance imaging and photodynamic therapy *in vitro*. Nanoscale **4**, 4611–4623 (2012)

137. Y. Liu, M. Chen, T.Y. Cao, Y. Sun, C.Y. Li, Q. Liu, T.S. Yang, L.M. Yao, W. Feng, F.Y. Li, A cyanine-modified nanosystem for in vivo upconversion luminescence bioimaging of methylmercury. J. Am. Chem. Soc. **135**, 9869–9876 (2013)
138. C.-J. Cailing, J.-C. Boyer, N.R. Branda, Remote-control photoswitching using NIR light. J. Am. Chem. Soc. **131**, 10838–10839 (2009)
139. J.-C. Boyer, C.-J. Carling, B.D. Gates, N.R. Branda, Two-way photoswitching using one type of near-infrared light, upconverting nanoparticles, and changing only the light intensity. J. Am. Chem. Soc. **132**, 15766–15772 (2010)
140. Y.M. Yang, Q. Shao, R.R. Deng, C. Wang, X. Teng, K. Cheng, Z. Cheng, L. Huang, Z. Liu, X.G. Liu, B.G. Xing, In vitro and in vivo uncaging and bioluminescence imaging by using photocaged upconversion nanoparticles. Angew. Chem. Int. Ed. **51**, 3125–3129 (2012)
141. L. Wang, H. Dong, Y.N. Li, C.M. Xue, L.D. Sun, C.H. Yan, Q. Li, Reversible near-infrared light directed reflection in a self-organized helical superstructure loaded with upconversion nanoparticles. J. Am. Chem. Soc. **136**, 4480–4483 (2014)
142. B.W. Wang, S.D. Jiang, X.T. Wang, Magnetic molecular materials with paramagnetic lanthanide ions. Sci. China Ser. B **52**, 1739–1758 (2009)
143. Q. Su (ed.), *Chemistry of Rare Earths* (Henan Science and Technology Press, Zhengzhou, 1993)
144. M. Bottrill, L.K. Nicholas, N.J. Long, Lanthanides in magnetic resonance imaging. Chem. Soc. Rev. **35**, 557–571 (2006)
145. P. Caravan, Strategies for increasing the sensitivity of gadolinium based MRI contrast agents. Chem. Soc. Rev. **35**, 512–523 (2006)
146. C. Geraldes, S. Laurent, Classification and basic properties of contrast agents for magnetic resonance imaging. Contrast Media Mol. Imaging **4**, 1–23 (2009)
147. Z.J. Zhou, Z.H. Zhao, H. Zhang, Z.Y. Wang, X.Y. Chen, R.F. Wang, Z. Chen, J.H. Gao, Interplay between longitudinal and transverse contrasts in Fe_3O_4 nanoplates with (111) exposed surfaces. ACS Nano **8**, 7976–7985 (2014)
148. P.J. Klemm, W.C. Floyd, D.E. Smiles, J.M.J. Frechet, K.N. Raymond, Improving T_1 and T_2 magnetic resonance imaging contrast agents through the conjugation of an esteramide dendrimer to high-water-coordination Gd(III) hydroxypyridinone complexes. Contrast Media Mol. Imaging **7**, 95–99 (2012)
149. S. Aime, M. Fasano, E. Terreno, Lanthanide(III) chelates for NMR biomedical applications. Chem. Soc. Rev. **27**, 19–29 (1998)
150. P. Caravan, J.J. Ellison, T.J. McMurry, R.B. Lauffer, Gadolinium(III) chelates as MRI contrast agents: Structure, dynamics, and applications. Chem. Rev. **99**, 2293–2352 (1999)
151. H.B. Na, I.C. Song, T. Hyeon, Inorganic nanoparticles for MRI contrast agents. Adv. Mater. **21**, 2133–2148 (2009)
152. M.A. McDonald, K.L. Watkin, Small particulate gadolinium oxide and gadolinium oxide albumin microspheres as multimodal contrast and therapeutic agents. Invest. Radiol. **38**, 305–310 (2003)
153. F. Chen, W. Bu, S. Zhang, J. Liu, W. Fan, L. Zhou, W. Peng, J. Shi, Gd^{3+}-ion-doped upconversion nanoprobes: relaxivity mechanism probing and sensitivity optimization. Adv. Funct. Mater. **23**, 298–307 (2013)
154. M. Rohrer, H. Bauer, J. Mintorovitch, M. Requardt, H.J. Weinmann, Comparison of magnetic properties of MRI contrast media solutions at different magnetic field strengths. Invest. Radiol. **40**, 715–724 (2005)
155. J.Y. Park, M.J. Baek, E.S. Choi, S. Woo, J.H. Kim, T.J. Kim, J.C. Jung, K.S. Chae, Y. Chang, G.H. Lee, Paramagnetic ultrasmall gadolinium oxide nanoparticles as advanced T_1 MR1 contrast agent: account for large longitudinal relaxivity, optimal particle diameter, and in vivo T_1 MR images. ACS Nano **3**, 3663–3669 (2009)
156. N.J.J. Johnson, W. Oakden, G.J. Stanisz, R.S. Prosser, F.C.J.M. van Veggel, Size-tunable, ultrasmall $NaGdF_4$ nanoparticles: insights into their T_1 MRI contrast enhancement. Chem. Mater. **23**, 3714–3722 (2011)

157. H. Hifumi, S. Yamaoka, A. Tanimoto, D. Citterio, K. Suzuki, Gadolinium-based hybrid nanoparticles as a positive MR contrast agent. J. Am. Chem. Soc. **128**, 15090–15091 (2006)
158. H. Hifumi, S. Yamaoka, A. Tanimoto, T. Akatsu, Y. Shindo, A. Honda, D. Citterio, K. Oka, S. Kuribayashi, Dextran coated gadolinium phosphate nanoparticles for magnetic resonance tumor imaging. J. Mater. Chem. **19**, 6393–6399 (2009)
159. Y. Gossuin, A. Hocq, Q.L. Vuong, S. Disch, R.P. Hermann, P. Gillis, Physico-chemical and NMR relaxometric characterization of gadolinium hydroxide and dysprosium oxide nanoparticles. Nanotechnology **19**, 475102 (2008)
160. W. Ren, G. Tian, L. Zhou, W.Y. Yin, L. Yan, S. Jin, Y. Zu, S.J. Li, Z.J. Gu, Y.L. Zhao, Lanthanide ion-doped $GdPO_4$ nanorods with dual-modal bio-optical and magnetic resonance imaging properties. Nanoscale **4**, 3754–3760 (2012)
161. Y.C. Li, T. Chen, W.H. Tan, D.R. Talham, Size-dependent MRI relaxivity and dual imaging with $Eu_{0.2}Gd_{0.8}PO_4$ center dot H_2O nanoparticles. Langmuir **30**, 5873–5879 (2014)
162. G.K. Das, B.C. Heng, S.C. Ng, T. White, J.S.C. Loo, L. D'Silva, P. Padmanabhan, K.K. Bhokoo, S.T. Selvan, T.T.Y. Tan, Gadolinium oxide ultranarrow nanorods as multimodal contrast agents for optical and magnetic resonance imaging. Langmuir **26**, 8959–8965 (2010)
163. Y. Zhang, G.K. Das, V. Vijayaragavan, Q.C. Xu, P. Padmanabhan, K.K. Bhakoo, S.T. Selvan, T.T.Y. Tan, "Smart" theranostic lanthanide nanoprobes with simultaneous up-conversion fluorescence and tunable T_1-T_2 magnetic resonance imaging contrast and near-infrared activated photodynamic therapy. Nanoscale **6**, 12609–12617 (2014)
164. Y. Tian, H.Y. Yang, K. Li, X. Jin, Monodispersed ultrathin GdF_3 nanowires: Oriented attachment, luminescence, and relaxivity for MRI contrast agents. J. Mater. Chem. **22**, 22510–22516 (2012)
165. T. Paik, T.R. Gordon, A.M. Prantner, H. Yun, C.B. Murray, Designing tripodal and triangular gadolinium oxide nanoplates and self-assembled nanofibrils as potential multimodal bioimaging probes. ACS Nano **7**, 2850–2859 (2013)
166. M. Cho, R. Sethi, J.S.A. Narayanan, S.S. Lee, D.N. Benoit, N. Taheri, P. Decuzzi, V.L. Colvin, Gadolinium oxide nanoplates with high longitudinal relaxivity for magnetic resonance imaging. Nanoscale **6**, 13637–13645 (2014)
167. H. Hu, D. Li, S. Liu, M.Z. Wang, R. Moats, P.S. Conti, Z.B. Li, Integrin α2β1 targeted GdVO4: Eu ultrathin nanosheet for multimodal PET/MR imaging. Biomaterials **35**, 8649–8658 (2014)
168. H. Hu, S. Liu, D. Li, M.Z. Wang, R. Moats, H. Shan, P.S. Conti, Z.B. Li, The synthesis of lanthanide-doped $GdVO_4$ ultrathin nanosheets with great optical and paramagnetic properties for FRET biodetection and in vivo MR imaging. J. Mater. Chem. B **2**, 3998–4007 (2014)
169. M. Abdesselem, M. Schoeffel, I. Maurin, R. Ramodiharilafy, G. Autret, O. Clement, P.L. Tharaux, J.P. Boilot, T. Gacoin, C. Bouzigues, Multifunctional rare-earth vanadate nanoparticles: luminescent labels, oxidant sensors, and MRI contrast agents. ACS Nano **8**, 11126–11137 (2014)
170. D.H. Geschwind, G. Konopka, Neuroscience in the era of functional genomics and systems biology. Nature **461**, 908–915 (2009)
171. E. Terreno, D.D. Castelli, A. Viale, S. Aime, Challenges for molecular magnetic resonance imaging. Chem. Rev. **110**, 3019–3042 (2010)
172. L. Helm, Optimization of gadolinium-based MRI contrast agents for high magnetic-field applications. Future Med. Chem. **2**, 385–396 (2010)
173. M. Norek, J.A. Peters, MRI contrast agents based on dysprosium or holmium. Prog. Nucl. Magn. Reson. Spectrosc. **59**, 64–82 (2011)
174. M. Norek, E. Kampert, U. Zeitler, J.A. Peters, Tuning of the size of Dy_2O_3 nanoparticles for optimal performance as an MRI contrast agent. J. Am. Chem. Soc. **130**, 5335–5340 (2008)
175. S. Viswanathan, Z. Kovacs, K.N. Green, S.J. Ratnakar, A.D. Sherry, Alternatives to gadolinium-based metal chelates for magnetic resonance imaging. Chem. Rev. **110**, 2960–3018 (2010)

176. G.K. Das, N.J.J.Johnson, J. Cramen, B. Blasiak, P. Latta, B.Tomanek, C.J.M. van Veggel, $NaDyF_4$ nanoparticles as T_2 contrast agents for ultrahigh field magnetic resonance imaging. J. Phys. Chem. Lett. **3**, 524–529 (2012)
177. H. Wang, Z. Yi, L. Rao, H.R. Liu, S.J. Zeng, High quality multi-functional $NaErF_4$ nanocrystals: structure-controlled synthesis, phase-induced multi-color emissions and tunable magnetic properties. J. Mater. Chem. C **1**, 5520–5526 (2013)
178. H. Wang, W. Lu, T. Zeng, Z. Yi, L. Rao, H. Liu, S. Zeng, Multi-functional NaErF4: Yb nanorods: enhanced red upconversion emission, in vitro vell, in vivo X-ray, and T2-weighted magnetic resonance imaging. Nanoscale **6**, 2855–2860 (2014)
179. A. Xia, X. Zhang, J. Zhang, Y.Y. Deng, Q. Chem, S. S. Wu, X. H. Huang, J. Shen. Enhanced dual contrast agent, Co^{2+}-doped $NaYF_4$:Yb^{3+}, Tm^{3+} nanorods, for near infrared-to-near infrared upconversion luminescence and magnetic resonance imaging. Biomaterials **35**, 9167–9176 (2014)
180. K. Kattel, J.Y. Park, W. Xu, H.G. Kim, E.J. Lee, B.A. Bony, W.C. Heo, S. Jin, J.S. Baeck, Y. Chang, Paramagnetic dysprosium oxide nanoparticles and dysprosium hydroxide nanorods as T_2 MRI contrast agents. Biomaterials **33**, 3254–3261 (2012)
181. K. Kattel, J.Y. Park, W. Xu, B.A. Bony, W.C. Heo, T. Tegafaw, C.R. Kim, M.W. Ahmad, S. Jin, J.S. Baeck, Surface coated $Eu(OH)_3$ nanorods: a facile synthesis, characterization, MR relaxivities and in vitro cytotoxicity. J. Nanosci. Nanotechnol. **13**, 7214–7219 (2013)
182. J. Zhou, Z.G. Lu, G.G. Shan, S.H. Wang, Y. Liao, Gadolinium complex and phosphorescent probe-modified $NaDyF_4$ nanorods for T_1- and T_2-weighted MRI/CT/phosphorescence multimodality imaging. Biomaterials **35**, 368–377 (2014)
183. M.J. Bailey, R. van der Weegen, P.J. Klemm, S.L. Baker, B.A. Helms, Stealth rare earth oxide nanodiscs for magnetic resonance imaging. Adv. Healthc. Mater. **1**, 437–442 (2012)
184. A. Trovarelli, A.C.D. Leitenburg, M. Boaro, G. Dolcetti, The utilization of ceria in industrial catalysis. Catal. Today. **50**, 353–367 (1999)
185. Z.L. Wang, X.D. Feng, Polyhedral shapes of CeO_2 nanoparticles. J. Phys. Chem. B **107**, 13563–13566 (2003)
186. D.S. Zhang, X.J. Du, L.Y. Shi, R.H. Gao, Shape-controlled synthesis and catalytic application of Ceria nanomaterials. Dalton Trans. **41**, 14455–14475 (2012)
187. E. Shoko, M.F. Smith, R.H. McKenzie, Charge distribution near bulk oxygen vacancies in cerium oxides. J. Phys.: Condens. Matter **22**, 223201–223218 (2010)
188. X.W. Liu, K.B. Zhou, L. Wang, B.Y. Wang, Y.D. Li, Oxygen vacancy clusters promoting reducibility and activity of ceria nanorods. J. Am. Chem. Soc. **131**, 3140–3141 (2009)
189. L. Vivier, D. Duprez, Ceria-based solid catalysts for organic chemistry. ChemSusChem. **3**, 654–678 (2010)
190. J.C. Conesa, Computer modeling of surfaces and defects on cerium dioxide. Surf. Sci. **339**, 337–352 (1995)
191. D.C. Sayle, S.A. Maicaneanu, G.W. Watson, Atomistic models for CeO_2 (111), (110), and (100) nanoparticles, supported on yttrium-stabilized zirconia. J. Am. Chem. Soc. **124**, 11429–11439 (2002)
192. E. Aneggi, C.D. Leitenburg, J. Llorca, A. Trovarelli, Higher activity of diesel soot oxidation over polycrystalline ceria and ceria–zirconia solid solutions from more reactive surface planes. Catal. Today **197**, 119–126 (2012)
193. C.S. Pan, D.S. Zhang, L.Y. Shi, J.H. Fang, Template-free synthesis, controlled conversion, and CO oxidation properties of CeO_2 nanorods, nanotubes, nanowires, and nanocubes. Eur. J. Inorg. Chem. **2008**, 2429–2436 (2008)
194. X. Wang, Z.Y. Jiang, B.J. Zheng, Z.X. Xie, L.S. Zheng, Synthesis and shape-dependent catalytic properties of CeO_2 nanocubes and truncated octahedral. CrystEngComm **14**, 7579–7582 (2012)
195. X. W. Lu, X.Z. Li, J.C. Qian, Z.G. Chen, The surfactant-assisted synthesis of CeO_2 nanowires and their catalytic performance for CO oxidation. Powder Technol. **239**, 415–421 (2013)

196. C.S. Pan, D.S. Zhang, L.Y. Shi, CTAB assisted hydrothermal synthesis, controlled conversion and CO oxidation properties of CeO_2 nanoplates, nanotubes, and nanorods. J. Solid State Chem. **181**, 1298–1306 (2008)
197. X.Z. Li, F. Chen, X.W. Lu, C.Y. Ni, X.B. Zhao, Z.G. Chen, Layer-by-layer synthesis of hollow spherical CeO_2 templated by carbon spheres. J. Porous Mater. **17**, 297–303 (2010)
198. C. Ho, J.C. Yu, T. Kwong, A.C. Mak, S.Y. Lai, Morphology-controllable synthesis of mesoporous CeO_2 nano- and microstructures. Chem. Mater. **17**, 4514–4522 (2005)
199. C.W. Sun, L.Q. Chen, Controllable synthesis of shuttle-shaped ceria and its catalytic properties for CO oxidation. Eur. J. Inorg. Chem. **2009**, 3883–3887 (2009)
200. X. Liang, J.J. Xiao, B.H. Chen, Y.D. Li, Catalytically stable and active CeO_2 mesoporous spheres. Inorg. Chem. **49**, 8188–8190 (2010)
201. Z.L. Wu, M.J. Li, J. Howe, H.M. Meyer, S.H. Overbury, Probing defect sites on CeO_2 nanocrystals with well-defined surface planes by Raman spectroscopy and O_2 adsorption. Langmuir **26**, 16595–16606 (2010)
202. Z.L. Wu, M.J. Li, S.H. Overbury, On the structure dependence of CO oxidation over CeO_2 nanocrystals with well-defined surface planes. J. Catal. **285**, 61–73 (2012)
203. Z.M. Tana, J. Li, H. Li, Y. Li, W. Shen, Morphology-dependent redox and catalytic properties of CeO_2 nanostructures: nanowires, nanorods and nanoparticles. Catal. Today **148**, 179–183 (2009)
204. B. Choudhury, P. Chetri, A. Choudhury, Oxygen defects and formation of Ce^{3+} affecting the photocatalytic performance of CeO_2 nanoparticles. RSC Adv. **4**, 4663–4671 (2014)
205. P.F. Ji, J.L. Zhang, F. Chen, M. Anpo, Ordered mesoporous CeO_2 synthesized by nanocasting from cubic *Ia3d* mesoporous MCM-48 silica: formation, characterization and photocatalytic activity. J. Phys. Chem. C **112**, 17809–17813 (2008)
206. X.H. Lu, D.Z. Zheng, J.Y. Gan, Z.Q. Liu, C.L. Liang, P. Liu, Y.X. Tong, Porous CeO_2 nanowires/nanowire arrays: electrochemical synthesis and application in water treatment. J. Mater. Chem. **20**, 7118–7122 (2010)
207. Z.J. Yan, J.J. Wei, H.X. Yang, L. Liu, H. Liang, Y.Z. Yang, Mesoporous CeO_2 hollowspheres prepared by Ostwald ripening and their environmental applications. Eur. Inorg. Chem. **2010**, 3354–3359 (2010)
208. X.H. Lu, T. Zhai, H.N. Cui, J.Y. Shi, S.L. Xie, Y.Y. Huang, C.L. Liang, Y.X. Tong, Redox cycles promoting photocatalytic hydrogen evolution of CeO_2 nanorods. J. Mater. Chem. **21**, 5569–5572 (2011)
209. M. Kobune, S. Sato, R. Takahashi, Surface-structure sensitivity of CeO_2 for several catalytic reactions. J. Mol. Catal. A: Chem. **279**, 10–19 (2008)
210. J.G. Lv, Y. Shen, L.M. Peng, X.F. Guo, W.P. Ding, Exclusively selective oxidation of toluene to benzaldehyde on ceria nanocubes by molecular oxygen. Chem. Commun. **46**, 5909–5911 (2010)
211. Y. Zhang, F. Hou, Y.W. Tan, CeO_2 nanoplates with a hexagonal structure and their catalytic applications in highly selective hydrogenation of substituted nitroaromatics. Chem. Commun. **48**, 2391–2393 (2012)
212. I. Celardo, J.Z. Pedersen, E. Traversa, Pharmacological potential of cerium oxide nanoparticles. Nanoscale **3**, 1411–1420 (2011)
213. C. Korsvik, S. Patil, S. Seal, W.T. Self, Superoxide dismutase mimetic properties exhibited by vacancy engineered ceria nanoparticles. Chem. Commun. **10**, 1056–1058 (2007)
214. T. Pirmohamed, J.M. Dowding, S. Singh, B. Wasserman, E. Heckert, A.S. Karakoti, J.E.S. King, S. Seal, W.T. Self, Nanoceria exhibit redox state-dependent catalase mimetic activity. Chem. Commun. **46**, 2736–2738 (2010)
215. Y. Xue, Q.F. Luan, D. Yang, X. Yao, K.B. Zhou, Direct evidence for hydroxyl radical scavenging activity of cerium oxide nanoparticles. J. Phys. Chem. C **115**, 4433–4438 (2011)
216. C.K. Kim, T. Kim, I.Y. Choi, M. Soh, D. Kim, Y.-J. Kim, H. Jang, H.-S. Yang, J.Y. Kim, H.-K. Park, Ceria nanoparticles that can protect against ischemic stroke. Angew. Chem. Int. Ed. **51**, 1–6 (2012)

217. J. Chen, S. Patil, S. Seal, J.F. Mcginnis, Rare earth nanoparticles prevent retinal degeneration induced by intracellular peroxides. Nat. Nanotechnol. **1**, 142–150 (2006)
218. A. Nel, T. Xia, L. Madler, N. Li, Toxic potential of materials at the nanolevel. Science **311**, 622–627 (2006)
219. S.J. Lin, X. Wang, Z.X. Ji, C.H. Chang, Y. Dong, H. Meng, Y.P. Liao, M.Y. Wang, T.B. Song, S. Kohan, Aspect ratio plays a role in the hazard potential of CeO_2 nanoparticles in mouse lung and zebrafish gastrointestinal tract. ACS Nano **8**, 4450–4464 (2014)
220. W.Q. Han, W. Wen, J.C. Hanson, X. Teng, N. Marinkovic, J.A. Rodriguez, One-dimensional ceria as catalyst for the low-temperature water-gas shift reaction. J. Phys. Chem. C **113**, 21949–21955 (2009)
221. C. Fang, D.S. Zhang, L.Y. Shi, R.H. Gao, H.R. Li, L.P. Ye, J.P. Zhang, Highly dispersed CeO_2 on carbon nanotubes for selective catalytic reduction of NO with NH_3. Catal. Sci. Technol. **3**, 803–811 (2013)
222. D. Barreca, A. Gasparotto, C. Maccato, C. Maragno, E. Tondello, E. Comini, G. Sberveglieri, Columnar CeO_2 nanostructures for sensor application. Nanotechnology **18**, 125502 (2007)
223. H. He, H.X. Dai, L.H. Ng, K.W. Wong, C.T. Au, Pd-, Pt-, and Rh-loaded $Ce_{0.6}Zr_{0.35}Y_{0.05}O_2$ three-way catalysts: an investigation on performance and redox properties. J. Catal. **206**, 1–13 (2002)
224. X. Yu, L. Kuai, B.Y. Geng, CeO_2/rGO/Pt sandwich nanostructure: rGO-Enhanced electron transmission between metal oxide and metal nanoparticles for anodic methanol oxidation of direct methanol fuel cells. Nanoscale **4**, 5738–5743 (2012)
225. H.P. Zhou, H.S. Wu, J. Shen, A.X. Yin, L.D. Sun, C.H. Yan, Thermally stable Pt/CeO_2 hetero-nanocomposites with high catalytic activity. J. Am. Chem. Soc. **132**, 4998–5011 (2010)
226. X.N. Lu, C.Y. Song, S.H. Jia, Z.S. Tong, X.L. Tang, Y.X. Teng, Low temperature selective catalytic reduction of NO_x with NH_3 over amorphous MnO_x catalysts prepared by three methods. Catal. Commun. **8**, 329–334 (2007)
227. R. Si, M. Flytzani-Stephanopoulos, Shape and crystal plane effects of nanoscale ceria on the activity of Au-CeO_2 catalysts for the water-gas shift reaction. Angew. Chem. Int. Ed. **47**, 2884–2887 (2008)